1-1-2010

Modeling the optical properties of a single gold nanorod for use in biomedical applications

Yevgeniy Davletshin
Ryerson University, davletshin@gmail.com

Modeling the optical properties of a single gold nanorod for use in biomedical applications

by

Yevgeniy Davletshin

B.Sc. Nuclear Physics, Al Farabi Kazakh National University, 2003,

A thesis

presented to Ryerson University

in partial fulfillment of the

requirements for the degree of

Master of Science

in the Program of

Biomedical Physics

Toronto, Ontario, Canada, 2010

I hereby declare that I am the sole author of this thesis.

I authorize Ryerson University to lend this thesis to other institutions or individuals for the purpose of scholarly research.

I further authorize Ryerson University to reproduce this thesis by photocopying or by other means, in total or in part, at the request of other institutions or individuals for the purpose of scholarly research.

Modeling the optical properties of a single gold nanorod for use in biomedical applications

Master of Science 2010

Yevgeniy Davletshin

Biomedical Physics

Ryerson University

Recent studies have shown that gold nanorods are highly effective agents for conversion of visible and near infrared (NIR) light into heat. Thermal therapy that utilizes this effect is called Plasmonic Photothermal Therapy (PPTT), where light absorption by photothermal agents (plasmon-resonant gold nanorods) causes kinetic energy to increase, resulting in heating of the area surrounding the agent. A primary understanding of optical and thermal properties of gold particles at nanoscale level is still unclear. Due to the limitations of current equipment for nanoparticle characterization, numerical methods and computational models are widely used to understand the physics at the nanoscale. In this thesis finite element analysis and spatial modulation spectroscopy were used to develop and test a computational model to characterize optical properties of a single gold nanorod.

Acknowledgements

I would like to thank my supervisor, Dr. Joseph Carl Kumaradas, for his support, guidance and trust in me. Two years of research under supervision of someone who knows a lot, but lets you choose your own destiny taught me the wisdom of decisions making.

Additionally I would like to thank my supervisory committee members for advising and questioning me on my project: Dr. Micheal C. Kolios and Dr. Warren C.W. Chan.

Futhermore, I would like to thank all members of our group: Shermiyah Baguisa, Thu Lee (Amanda) Tran, Christine Tarapacki, Yasaman Nobahar and Dr. Tanya Hauck; that were always enthusiastic and keen to work in the lab.

Special words of appreciation to the international group that I met, worked with and became friends with at the FemtoNanoOptics group, Université Claude Bernard Lyon 1: Anna Lombardi, Vincent Juvé, Denis Mongin, Dr. Mahdi Harb, Dr. Hatim Baida, Dr. Natalia Del Fatti, Dr. Fabrice Vallee, Dr. Paolo Maioli, Dr. Aurelien Crut and Maria Fernanda Cardinal. Special thanks to my friend Hatim, who went through all troubles of speaking French on my behalf in Lyon's official offices.

And finally I would like to thank my friends, the graduate students and the physics department for making this journey joyful and fun.

Dedication

Dedicated to my family

Contents

List of Tables

List of Figures

Notations

A	Scalar quantity.
$\tilde{a}$	Complex quantity.
$\mathbf{A}$	Vector quantity.
$\hat{a}$	Basis/unit vector.

Operators

$\tilde{A}^*$	Complex conjugate of $\tilde{A}$.
∇A	Gradient of A.
$\nabla \cdot \mathbf{A}$	Divergence of $\mathbf{A}$.
$\nabla \times \mathbf{A}$	Curl of $\mathbf{A}$.
$\lvert\mathbf{A}\rvert$	Magnitude of $\mathbf{A}$.
$\Re(a)$	Real part of a.
$\Im(a)$	Imaginary part of a.

Symbols

$\mathbf{E}, \mathbf{E}_{\text{inc}}, \mathbf{E}_{\text{sca}}$	Total, incident and scattered electric field ($\text{V} \cdot \text{m}^{-1}$).
$\mathbf{H}, \mathbf{H}_{\text{sca}}$	Total and scattered magnetic field ($\text{A} \cdot \text{m}^{-1}$).
$\mathbf{B}$	Magnetic induction (T).
$\mathbf{D}$	Electric induction ($\text{C} \cdot \text{m}^{-2}$).
$\mathbf{J}$	Current density ($\text{A} \cdot \text{m}^{-2}$).
$\mathbf{S}, \mathbf{S}_{\mathbf{av}}$	Poynting and time-averaged Poynting vector ($\text{W} \cdot \text{m}^{-2}$).
$\mathbf{P}$	Polarization ($\text{C} \cdot \text{m}^{-2}$).
i	Imaginary number defined as $\sqrt{-1}$.
κ	Wavenumber (m^{-1}).
κ_0	Wavenumber of free space (m^{-1}).

λ	Wavelength of light (m).
ω	Wave's angular frequency ($\mathrm{rad} \cdot \mathrm{s}^{-1}$).
c_0	Speed of light in vacuum (m).
ρ	Total charge density ($\mathrm{C} \cdot \mathrm{m}^{-3}$).
ϵ	Electrical permittivity ($\mathrm{F} \cdot \mathrm{m}^{-1}$).
$\tilde{\epsilon_\mathrm{r}}$	Complex relative permittivity (1).
ϵ_0	Electrical permittivity of free space ($\mathrm{F} \cdot \mathrm{m}^{-1}$).
χ	Electric susceptibility (1).
σ	Electrical conductivity ($\mathrm{S} \cdot \mathrm{m}^{-1}$).
μ	Magnetic permeability ($\mathrm{H} \cdot \mathrm{m}^{-1}$).
$\tilde{\mu_\mathrm{r}}$	Complex relative permeability (1).
μ_0	Magnetic permeability of free space($\mathrm{H} \cdot \mathrm{m}^{-1}$).
χ_m	Magnetic susceptibility (1).
$\tilde{n}$	Complex index of refraction (1).
n	Real part of the complex index of refraction (1).
k	Extinction coefficient (1).
σ_ext	Extinction cross-section (m^2).
σ_abs	Absorption cross-section (m^2).
σ_sca	Scattering cross-section (m^2).
ρ_n	Number density (m^{-3}).
I_0	Intensity of incident light (W).
μ_a	Absorption coefficient (m^{-1}).
μ_s	Scattering coefficient (m^{-1}).
m_e	Free electron's mass (kg).
e	Electron's charge (C).
Γ	Phenomenological damping constant (s^{-1}).
ω_p	Plasma frequency of electron gas ($\mathrm{rad} \cdot \mathrm{s}^{-1}$).
χ^IB	Interband susceptibility (1).
χ^D	Drude (free electrons) susceptibility (1).
γ_0	Bulk damping constant (s^{-1}).
v_F	Fermi velocity ($\mathrm{m} \cdot \mathrm{s}^{-1}$).
l_∞	Bulk mean free path (m).

L_{eff}	Effective mean free path length (m).
A	Broadening parameter (1).
η	Radiation damping constant ($\text{fs}^{-1} \cdot \text{nm}^{-3}$).

Abbreviations

ABC	Absorbing boundary conditions.
AR	Aspect ratio.
DDA	Discrete dipole approximation.
FDTD	Finite difference time domain.
FEM	Finite element method.
FWHM	Full width half maximum.
GNR	Gold nanorod.
NIR	Near infrared.
PDE	Partial differential equations.
PEC	Perfect electric conductor.
PMC	Perfect magnetic conductor.
PML	Perfect matched layer.
PPTT	Plasmonic photothermal therapy.
SMS	Spatial modulation spectroscopy.
SPR	Surface plasmon resonance.
TEM	Transmission electron microscopy.

Chapter 1

Introduction

The history of thermal therapy starts more than 3000 years ago. At that time warm baths were used to cure different diseases. In present times thermal therapy is used primarily as a cancer treatment [1] during which tissue is exposed to high temperatures (45-60 °C) inducing cell damage and cell death. It can also be combined with other modalities of cancer therapy to increase the sensitivity of cancer cells to these therapies, enhancing their overall treatment effect.

For localized thermal therapy, energy can be delivered to the target region using ultrasound [2], radiofrequency electrical currents [3], microwaves [4] or laser [5]. Recent studies of optical properties of gold nanoparticles have provided motivation for new type of targeted thermal therapy. The tunable optical resonance and strong absorbance of light in the visible and infrared spectrum by gold nanoparticles [6, 7, 8] makes them suitable for heat dose delivery to a tumor region [9, 10, 11, 12, 13]. The process of light absorption by gold nanoparticles and the subsequent heating of the region around them have been called Plasmonic Photothermal Therapy (PPTT) [14].

Optical properties of gold nanoparticles that are used during PPTT will affect the amount of heating produced. Gold nanoshells [15], nanospheres [16] and nanorods [17] are the key nanoparticles that have been used in initial investigations of the PPTT feasibility. Among them gold nanorods are the ones that could be easily tuned to near infrared (NIR) wavelengths of the laser and produce more heating [18, 19] when the same amount of gold per volume is used.

1.1 Gold nanorods

A gold nanorod (GNR), due to its elongation in one direction, has two distinct plasmon resonances, called the transverse and longitudinal peaks (see Figure 1.1). The later one, is of more interest for the medical applications since it has higher absorption cross-section and can be tuned to NIR wavelengths where the biological tissue are more transparent to NIR light. There are several parameters that correspond to the location and amplitude of the longitudinal plasmon resonance peak [20, 21]: the dielectric function of the gold, end-tip shape, aspect ratio and concentration of the rods and dielectric properties of the medium. It is important to account and optimize these parameters when choosing gold nanorods for a specific medical application. Due to difficulties in gold nanorod experimental characterization on a single particle level it is vital to have a numerical model that will accurately predict optical response of a single gold nanorod. Ungureanu *et. al.* [22] emphasized the importance of input parameters such as the dielectric function and the shape of gold nanorod for numerical modeling, and showed discrepancy in the results of experimental and theoretical spectra comparison, due to choice of these parameters.

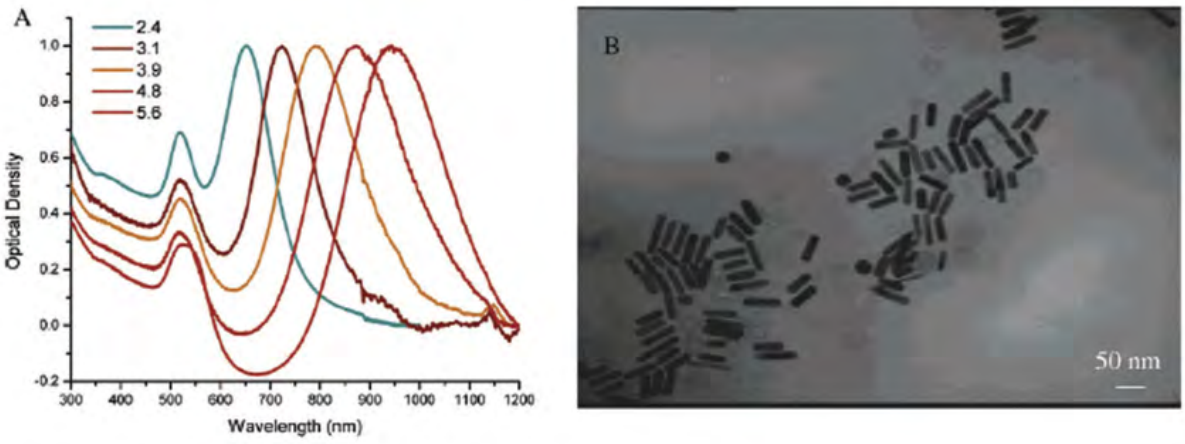

Figure 1.1: (A) Surface plasmon absorption spectra of gold nanorods of different aspect ratios, showing the sensitivity of the strong longitudinal band to the aspect ratios of the nanorods. (B) TEM image of nanorods of aspect ratio of 3.9, the absorption spectrum of which is shown as the orange curve in panel A. Reprinted from ref. [23].

1.2 Computational electromagnetics

Computational electromagnetic methods [24] are numerical techniques to model interaction of physical matter with electromagnetic fields. It typically involves a modeling of the light propagation, scattering and attenuation, through the medium or object. In this thesis the light scattered and absorbed by a gold nanorod is of main interest. Since an analytical solution for scattering problem exists only for simple geometries like a spherical object and an infinitely long cylinder, a numerical technique was used to find an approximate solution. Some of the widely used computational electromagnetic methods are the discrete dipole approximation (DDA), finite difference time domain (FDTD) method and finite element method (FEM).

1.2.1 Discrete dipole approximation

The Discrete Dipole Approximation method [25] is an integral equation method, where object that is scattering the electromagnetic wave is approximated by a number of dipoles. Each dipole is a polarizable point directly related to the local value of the polarization vector and located on a cubic lattice with interdipole distance d. This distance d is determined by the number of dipoles N used and volume V of the particle, and defined as $V = Nd^3$. The number of dipoles N needs to be chosen so it satisfies the accuracy criterion $|\tilde{n}|\,\kappa d < 0.5$, where $\tilde{n}$ is the complex refractive index of the target material and $\kappa = 2\pi/\lambda$ is the wavenumber for light with wavelength λ. The DDA is less precise with large values of the refractive index. To overcome this limitation, a larger number of dipoles needs to be needed, that consequently will lead to increase in the computational time. In addition, the "staircase" (Figure 1.2) representation of the curved geometry can affect the DDA accuracy. DDSCAT 7.1 [26] is one of the freely available open-source Fortran-90 codes that is widely used today to calculate an approximate solution for scattering and absorption of electromagnetic waves by targets with arbitrary geometries [22, 27] and complex refractive index.

1.2.2 Finite-difference time-domain method

The finite-difference time-domain method is a direct method to solve Maxwell's curl equations [28] in differential form. It was first developed by Yee [29], and currently

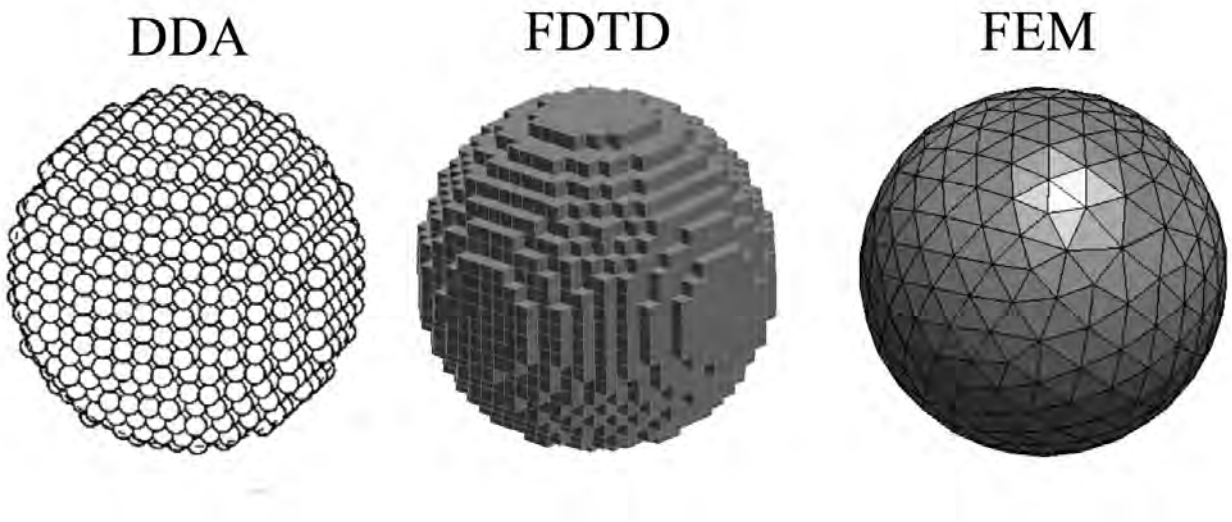

Figure 1.2: Examples of mesh generation with DDA, FDTD and FE methods

widely used for the analysis of electromagnetic wave interaction with nanostructures [30, 31]. In the FDTD method, Maxwell's equations are descritized in both the space and time domains in order to find the electric and magnetic fields as a function of space and time. The FDTD method is one of the simplest methods to implement and can be applied to inhomogeneous, anisotropic and arbitrary shaped geometries. Like the DDA, the FDTD method employs "staircase" meshing grid (Figure 1.2) that will require very fine refinement to obtain an appropriate solution at the edges of curved surfaces.

1.2.3 Finite element method

The finite element method was first introduced in the 1940's [32], when there was a need of solving complex elasticity and structural mechanics problems. In the late 1960's with the papers by Silvester [33] and Arlett *et. al.* [34] the finite element method was introduced to electrical engineering addressing applications related to waveguide and cavity analysis. It is a numerical technique that finds an approximate solution of the partial differential equations (PDE) by discretization of the computational domain into smaller finite triangular elements (Figure 1.2) to produce a system of ordinary differential equations. In the past decades the FEM was widely used in electromagnetic problems [35, 36, 37], primarily to solve set of Maxwell's equations with appropriate boundary

conditions.

There are several advantages of the FEM over other methods in computational electromagnetics. The FEM as well as DDA and FDTD methods can be applied to inhomogeneous, anisotropic and arbitrary shaped objects [36]. Furthermore, since the FEM can use unstructured meshes, it produces higher resolution for arbitrary shaped objects where a rapid variation of the solution can exist. Another distinct feature of the FEM, compared to the DDA, is it's applicability to solve different PDEs for the same geometry and couple several physical problems together with the same method. More detailed explanation of the FEM will be given in the methods chapter along with the description of the computational model.

1.3 Hypothesis, aims and outline of the thesis

For biomedical applications of the gold nanorods, it is important to tailor the nanorod's optical properties to satisfy specific requirements e.g. imaging, sensing or therapy. Modeling of the nanorod's optical properties [22] will require initial input parameters such as the size and shape of the nanorod and a dielectric function of gold.

With the advances in nanoscale chemistry, the best size and shape of the nanorod for specific applications, can be determined by the numerical model predictions for the following chemical synthesis. On the other hand the dielectric function of gold is a *static* input parameter that can not be altered to produce new properties of the particle. As will be discussed in the following chapter, the dielectric function of gold at the nanoscale is different from the experimentally obtained bulk values and is changing as a function of nanoparticle's size. This fact introduces an unknown into the modeling of the gold nanoparticle optical properties. However, it can be solved as an inverse problem, when optical properties of the nanoparticle obtained experimentally are then fitted with the numerical model to deduce the size-corrected dielectric function of gold.

Scatter-based spectroscopic techniques [38, 39] can yield precise spectral information of a nanorod, but often lack quantitative information of single nanorod absorption. The methods also have a limited access for performing electron microscopy on the same imaged particle. Recently, an absorption-based technique called spatial modulation spectroscopy (SMS) [40, 41] has shown promissing results in detecting, imaging and obtaining

quantitative extinction spectra of a single nanoparticle. Muskens *et. al.* [41] were able to determine the absolute value of the extinction cross-section of a single nanorod and were able to fit experimental data with results of numerical modeling. Modeling was done by placing gold nanorod in a homogeneous environment with an averaged value of the refractive index between air and a substrate, and dimensions (size and shape of GNRs tip-end) chosen to fit experimental data. Lack of experimental size determination of the SMS imaged GNR, introduced many fitting parameters into modeling that can be reduced by the use of TEM grid and follow up electron microscopy of the same GNR.

Therefore, it is hypothesized that *SMS combined with TEM can be used to build and validate an accurate finite element model of the optical behavior of a single GNR.* There are two specific aims that were pursued in this thesis:

1. To build a FEM model for single gold nanorod characterization and validate this model against a single gold nanorod SMS measurement.

2. To determine the size corrections for the dielectric function of gold for a single gold nanorod.

The following steps were taken in the thesis to achieve these aims:

- Development of the finite element model of the experimental (SMS) setup.

- Validation of the numerical model against analytical solution and experimental data.

- Quantitative characterization of the optical properties of a single gold nanorod using the SMS technique.

- Size and shape evaluation of the imaged gold nanorod using electron microscopy.

- Evaluation of the size corrections to the bulk dielectric constant of gold, by modeling the optical response of a single nanorod measured with SMS and correlated with TEM techniques.

The remainder of this thesis presents work carried out to model and characterize optical response of a single gold nanorod with numerical and experimental methods.

Chapter 2 presents the basic electrodynamic and solid-state physics theory required to understand the interaction of an electromagnetic field with matter and the properties of colloidal metal particles. The experimental and numerical methods are presented in chapter 3. The validation of the numerical model along with results of size correction to the bulk dielectric function evaluation is presented in chapter 4. Chapter 5 provides a summary of the results with the future work plan.

Chapter 2

Theoretical background

The understanding of the single nanoparticle optical response to the incident light requires and understanding of the physics of surface plasmon resonance and the properties of colloidal gold particles. The basic concepts of these disciplines will be introduced in this chapter. It will include Maxwell's equations and classical electrodynamics for the description of the optical properties of nanoparticles, and an overview of solid-state theory for the explanation of the material properties.

2.1 Theory of surface plasmon resonance

For more than several centuries, optical properties of noble nanoparticles attracted minds of the human race. One of the famous examples of the noble nanoparticles application is the Lycurgus cup (Figure 2.1). Dichroic glass of this cup was made with the use of the gold and silver nanoparticles that gives different bright colors to the cup under different light illumination. If the light shone through the glass, the cup appears red, but if the cup is illuminated with the reflected light, then it appears green. The color of the Lycurgus cup is determined by the embedded gold and silver nanoparticles and localized surface plasmon resonance (SPR) of these particles.

Electron microscopy of the dichroic glass revealed that most of the gold and silver nanoparticles embedded into the glass have spherical shape with diameters ranging from 5 to 60 nm. The shape and size of these nanoparticles will determine its localized surface plasmon resonance in the 400-600 nm range of the electromagnetic wavelengths

Figure 2.1: The Lycurgus cup. Late Roman empire 4th Century AD. (British Museum, London)

which correspond to the color from violet to green of the visible spectrum (Figure 2.2). Furthermore, when the light shines through the Lycurgus cup, one will see only the red component of the spectrum since green and blue light is absorbed or scattered by the gold and silver nanoparticles. On the other hand if the light is reflected by the dichroic glass, the cup will appear green since the green light will be back scattered by the nanoparticles and red light will travel through the glass unperturbed.

As was shown above, the color of the cup is determined by the light interaction with plasmonic nanoparticles. When a metal particle undergos excitation due to interactions with the light, incident photons will be scattered and absorbed by the electrons of the particle lattice and will cause an enhancement of the local electromagnetic field. The collective dipolar oscillations of the free conduction electrons (plasmons) due to this excitation are called surface plasmons [42]. The photo excitation of the surface plasmons in the particles with a diameter less than the wavelength of light is denoted as a localized surface plasmon resonance [42].

The phenomena of SPR can be described via classical electrodynamics where the

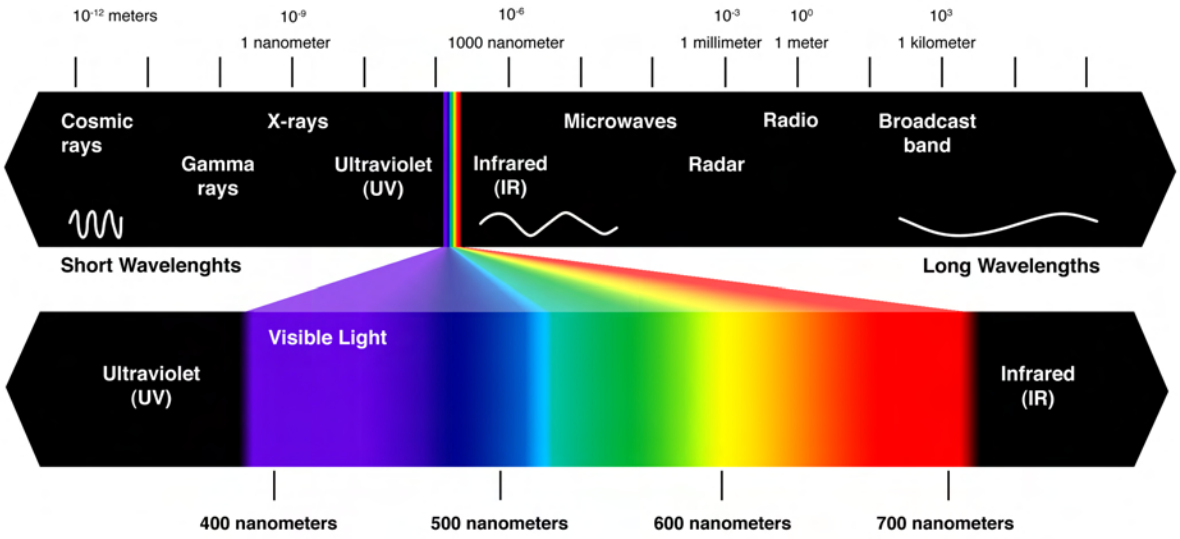

Figure 2.2: The electromagnetic spectrum. Adopted from http://blog.widen.com.

behavior of the electromagnetic field is governed by the macroscopic Maxwell's equations (2.1-2.4) [28]. The four main Maxwell's equations that define the fields which are generated by currents and charges in matter, and equation of charge conservation are

Faraday's law

$$\nabla \times \mathbf{E} = -\frac{\partial \mathbf{B}}{\partial t} \tag{2.1}$$

Maxwell-Ampere law

$$\nabla \times \mathbf{H} = \frac{\partial \mathbf{D}}{\partial t} + \mathbf{J} \tag{2.2}$$

Gauss's law

$$\nabla \cdot \mathbf{D} = \rho \tag{2.3}$$

Gauss's law for magnetism

$$\nabla \cdot \mathbf{B} = 0 \tag{2.4}$$

equation of charge conservation

$$\nabla \cdot \mathbf{J} = -\frac{\partial \rho}{\partial t}. \tag{2.5}$$

In these set of equations four macroscopic fields: the dielectric displacement $\mathbf{D}$, the electric field $\mathbf{E}$, the magnetic field $\mathbf{H}$, the magnetic induction $\mathbf{B}$, and the external charge ρ and current density $\mathbf{J}$ are linked together. In order to describe the behavior of matter under the influence of the external fields, the so-called constitutive relations need to be used:

$$\mathbf{D} = \epsilon_0 \tilde{\epsilon_\mathrm{r}} \mathbf{E}, \tag{2.6}$$

$$\mathbf{B} = \mu_0 \tilde{\mu_\mathrm{r}} \mathbf{H}, \tag{2.7}$$

and

$$\mathbf{J} = \sigma \mathbf{E}, \tag{2.8}$$

where constants $\epsilon_0 \approx 8.854 \times 10^{-12}$ F/m and $\mu_0 \approx 1.257 \times 10^{-6}$ H/m are the electric permittivity and magnetic permeability of free space, respectively, and $\tilde{\epsilon_\mathrm{r}}$, $\tilde{\mu_\mathrm{r}}$, $\mathbf{J}$ and σ are complex relative permittivity[1] and complex relative permeability[2] of the medium, conduction current density and dielectric conductivity, respectively. The conductivity σ can be also rewritten in more general form as a complex quantity[3] $\tilde{\sigma} = \sigma_1 + i\sigma_2$ to include the phase shift of the conduction and the bound currents, due to the fact that the response of the medium can have a time delay with respect to the applied field; where σ_1 describes an energy loss and σ_2 describe a change in phase of the electromagnetic wave.

As it is seen from (2.6 - 2.7) the electric and magnetic flux densities depend on material properties ($\tilde{\epsilon_\mathrm{r}}$ and $\tilde{\mu_\mathrm{r}}$) where electric and magnetic fields exists. The complex relative permittivity $\tilde{\epsilon_\mathrm{r}}$ and complex relative permeability $\tilde{\mu_\mathrm{r}}$ related to the electric and magnetic polarization properties of the material through

$$\tilde{\epsilon_\mathrm{r}} = 1 + \tilde{\chi}, \tag{2.9}$$

and

$$\tilde{\mu_\mathrm{r}} = 1 + \tilde{\chi}_\mathrm{m}, \tag{2.10}$$

where $\tilde{\chi}$ and $\tilde{\chi}_\mathrm{m}$ are complex electric and complex magnetic susceptibilities, respectively.

[1]For a vacuum $\tilde{\epsilon_\mathrm{r}} = 1$

[2]In nonmagnetic medium $\tilde{\mu_\mathrm{r}} = 1$.

[3]Subscripts 1 and 2 in complex quantities are used to indicate real and imaginary part, respectively.

The complex electric permittivity $\tilde{\epsilon}$ and complex permeability $\tilde{\mu}$ are defined by

$$\tilde{\epsilon} = \epsilon_0 \tilde{\epsilon_{\mathrm{r}}} = \epsilon_0(1 + \tilde{\chi}), \tag{2.11}$$

and

$$\tilde{\mu} = \mu_0 \tilde{\mu_{\mathrm{r}}} = \mu_0(1 + \tilde{\chi}_{\mathrm{m}}), \tag{2.12}$$

where complex electric susceptibility $\tilde{\chi}$ defines the response of bound charges to a driving electric field and result in an electric polarization; and complex magnetic susceptibility define the degree of magnetization of a material in response to an applied magnetic field. Furthermore, with the use of complex dielectric susceptibility $\tilde{\chi}$, a linear relationship between polarization the $\mathbf{P}$ and the electric field $\mathbf{E}$ can be described by

$$\mathbf{P} = \epsilon_0 \tilde{\chi} \mathbf{E}, \tag{2.13}$$

where polarization $\mathbf{P}$ can be denoted as the volume density of electric dipole moments and represents the dielectric polarization of the material.

To show the relationship between the dielectric function and the conductivity, equation (2.2) in the absense of external currents and with the use of Ohm's law (2.8) and equation (2.6) can be rewritten as

$$\nabla \times \mathbf{H} = \sigma_1 \mathbf{E} - i\omega\epsilon_r\epsilon_0 \mathbf{E} = -i\omega\tilde{\epsilon}\mathbf{E}, \tag{2.14}$$

where the displacement term is assumed to have a harmonic time dependence $\partial \mathbf{D}/\partial t = -i\omega\mathbf{D}$, and the relative permittivity[4] have linear relationship with conductivity through

$$\tilde{\epsilon} = \epsilon_0\epsilon_r + i\frac{\sigma}{\omega} = \epsilon_1 + i\epsilon_2. \tag{2.15}$$

The complex index of refraction $\tilde{n}$ can be related to complex dielectric function $\tilde{\epsilon}$ [43] through:

$$\tilde{n} = n - ik = \sqrt{\tilde{\epsilon}}, \tag{2.16}$$

where k is an extinction coefficient and determines the optical absorption of an electromagnetic wave. As stated earlier, real part σ_1 of the complex conductivity describes the

[4] ϵ_r is a real part of relative permittivity.

energy loss and can be related to the power absorbed for a given amplitude of electric field through $P_{\mathrm{a}} = \sigma_1 |\mathbf{E}|^2$.

In nonmagnetic medium and with the absence of external charges and current densities, the combination of the curl equations (2.1-2.2) with the constitutive relations (2.6 - 2.8) yield

$$\nabla \left(\frac{1}{\tilde{\epsilon}} \mathbf{E} \cdot \nabla \tilde{\epsilon} \right) + \nabla \times \nabla \times \mathbf{E} = \mu_0 \epsilon_0 \tilde{\epsilon} \frac{\partial^2 \mathbf{E}}{\partial t^2}. \tag{2.17}$$

Assuming that the electric field is time harmonic $\mathbf{E}(\mathbf{r}, t) = \mathbf{E}(\mathbf{r})\, \mathrm{e}^{-i\omega t}$, and that spatial variation of the $\tilde{\epsilon}$ is negligible, so that (2.17) takes the form of the Helmholtz wave equation,

$$\nabla \times \nabla \times \mathbf{E} - \kappa_0^2 \tilde{\epsilon} \mathbf{E} = \mathbf{0}, \tag{2.18}$$

where $\kappa_0 = \omega \sqrt{\epsilon_0 \mu_0}$ is a wave number in vacuum. Solution of the Helmholtz wave equation (2.18) with appropriate boundary conditions will help to derive the spatial evolution of the electromagnetic field in the presence of matter. Thereby, with the use of classical electrodynamics (2.18), propagation of the electromagnetic excitations at the metal-dielectric interface can be described.

2.1.1 Boundary conditions

For a full mathematical description of the metal-dielectric interface with the Helmholtz wave equation (2.18), a set of boundary conditions should be imposed to account for the discontinuity of the electrical and magnetic fields at the boundary between medium 1 and medium 2

$$\hat{\mathbf{n}} \times (\mathbf{H}_1 - \mathbf{H}_2) = \mathbf{J}, \tag{2.19}$$

$$\hat{\mathbf{n}} \times (\mathbf{E}_1 - \mathbf{E}_2) = \mathbf{0}, \tag{2.20}$$

$$\hat{\mathbf{n}} \cdot (\mathbf{D}_1 - \mathbf{D}_2) = \rho, \tag{2.21}$$

$$\hat{\mathbf{n}} \cdot (\mathbf{B}_1 - \mathbf{B}_2) = 0, \tag{2.22}$$

where $\hat{\mathbf{n}}$ is the unit normal vector on the boundary.

To truncate the computational domain a perfect electric conductor (PEC) equation (2.23), a perfect magnetic conductor (PMC) equation (2.24) and an absorbing boundary

(ABC) equation (2.25), conditions are used:

$$\hat{\mathbf{n}} \times \mathbf{E} = 0, \tag{2.23}$$

$$\hat{\mathbf{n}} \times \mathbf{H} = 0, \tag{2.24}$$

and

$$\hat{\mathbf{n}} \times \mathbf{H} = \frac{1}{\sqrt{\mu_0 \epsilon_0}} \times \hat{\mathbf{n}} \times \hat{\mathbf{n}} \times \mathbf{E} + \hat{\mathbf{n}} \times \mathbf{H}_{\text{inc}} - \frac{1}{\sqrt{\mu_0 \epsilon_0}} \times \hat{\mathbf{n}} \times \hat{\mathbf{n}} \times \mathbf{E}_{\text{inc}}, \tag{2.25}$$

where $\mathbf{E}_{\text{inc}}$ and $\mathbf{H}_{\text{inc}}$ are the incident electric and magnetic fields, respectively.

2.1.2 Poynting vector and optical response of a single nanoparticle

The Poynting vector $\mathbf{S}$ represents the amount of power per unit area that a wave carries in the direction of its propagation. The time-averaged Poynting vector $\mathbf{S}_{\text{av}}$ (units of W/m^2), is given by

$$\mathbf{S}_{\text{av}} = \frac{1}{2} \Re(\mathbf{E} \times \mathbf{H}^*). \tag{2.26}$$

When light propagates in a medium it dissipates its energy by interaction with charged particles (electrons and atomic nuclei) of the matter. The optical response of a single gold nanorod to incident light is characterized by its absorption and scattering cross-section or the amount of energy absorbed by the nanorod (due to ohmic losses) and scattering per unit area. The absorption cross-section σ_{abs} of a single gold nanorod can be given as a fraction of integrated resistive heating over nanorod's volume V divided by the incident power density:

$$\sigma_{\text{abs}} = \frac{2}{c_0 \epsilon_0 n E_{\text{inc}}^2} \int_V \Re(\sigma \mathbf{E} \cdot \mathbf{E}^* - i\omega \mathbf{E} \cdot \mathbf{D}^*) dV, \tag{2.27}$$

where c_0, n and E_{inc} are speed of light in the vacuum, refractive index of the medium and magnitude of the incident electric field, respectively. The scattering cross-section σ_{sca}, on the other hand is a fraction of the outgoing electromagnetic energy flux over an

arbitrary boundary S surrounding the gold nanorod per the incident power density

$$\sigma_{\mathrm{sca}} = \frac{2}{c_0 \epsilon_0 n \mathrm{E}_{\mathrm{inc}}^2} \int_S \Re(\mathbf{E}_{\mathrm{sca}} \times \mathbf{H}_{\mathrm{sca}}^*) dS. \tag{2.28}$$

Experimentalists usually describe optical properties of nanoparticles by its extinction cross-section σ_{ext}, that combines effects of absorption and scattering:

$$\sigma_{\mathrm{ext}} = \sigma_{\mathrm{abs}} + \sigma_{\mathrm{sca}}. \tag{2.29}$$

For biomedical applications of gold nanorods, such as PPTT, the main interest lies in determining the scattering μ_{s} and absorption μ_{a} coefficients of a medium consisting of GNRs. These are directly related to the scattering, absorption and extinction cross-sections of a single GNR through

$$\mu_{\mathrm{s}} = \rho_{\mathrm{n}} \sigma_{\mathrm{sca}}, \tag{2.30}$$

and

$$\mu_{\mathrm{a}} = \rho_{\mathrm{n}} \sigma_{\mathrm{abs}}. \tag{2.31}$$

where ρ_{n} is the number density of the particles. The equations 2.30 and 2.31 are valid only for concentration of particles where coupling effects between two neighboring particles are insignificant and can be neglected. The extinction coefficient, $\mu_{\mathrm{e}} = \mu_{\mathrm{a}} + \mu_{\mathrm{s}}(1-g) = \rho_{\mathrm{n}} \sigma_{\mathrm{ext}}$,[5] can be related to the intensity loss, $I_{\mathrm{ext}}(z)$, of a parallel beam propagating through the medium via Beer-Lambert's law,

$$I_{\mathrm{ext}}(z) = I_0 \mathrm{e}^{\mu_{\mathrm{e}} z}, \tag{2.32}$$

where I_0 is the intensity of incident light.

2.2 The electrical properties of metal nanoparticles

The size of the nanoparticles plays an important role in their optical properties. Two regimes can be distinguished that differentiate size effects of the nanoparticles on frequency dependent dielectric function $\tilde{\epsilon}(\omega)$. The *extrinsic* size effect applies to the large

[5]The g is an anisotropy factor.

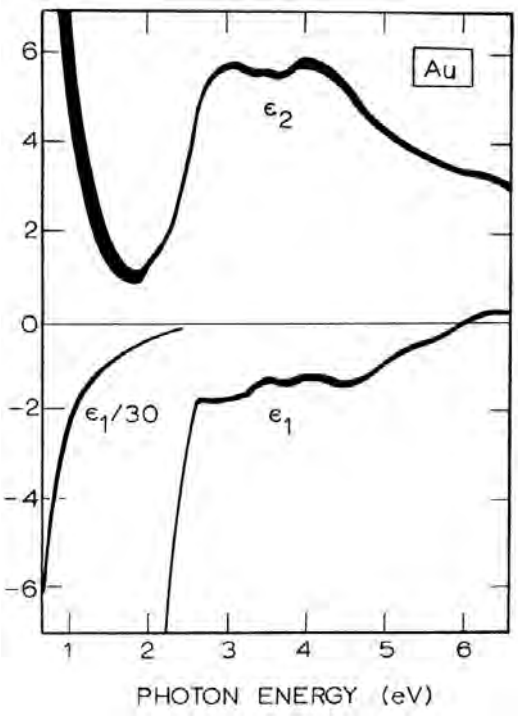

Figure 2.3: Dielectric constants for gold as a function of photon energy. The width of the curves is representative of the instrumental error. Reprinted from ref. [44]

nanoparticles, when dielectric function $\tilde{\epsilon}$ become a bulk dielectric function and independent of particle size, i.e. $\tilde{\epsilon}(\omega) = \tilde{\epsilon}_{\text{bulk}}(\omega)$. When the size of a nanoparticle becomes very small, the *intrinsic* size effects become dominant and the dielectric function varies as a function of particle radius R, i.e. $\tilde{\epsilon}(\omega) = \tilde{\epsilon}(\omega, R)$. In the following sections the bulk dielectric properties of metals and corrections to the bulk dielectric function due to the size of a nanoparticle are described.

2.2.1 Experimental values of bulk dielectric function

Over the past four decades the experimental data of Johnson and Christy [44] (Figure 2.3) has become a standard for the optical constants of noble metals. The experimental values of the complex refractive index, $\tilde{n} = n - ik$, were obtained from reflection and transmission measurements on vacuum-evaporated thin films. In case of the gold, three thicknesses of the thin film were used 18.6 nm, 34.3 nm and 45.6 nm. Comparison of the optical constants values from experiments with 34.3 nm and 45.6 nm thin films revealed no

thickness dependency (or *intrinsic* size effects) and agreed well within the estimation within experimental error. On the other hand, the values for the complex dielectric function $\tilde{\epsilon}$ in the measurements of 18.6 nm thick film were outside of the error estimates, compared to 34.3 nm and 45.6 nm film measurements. From these findings, it can be concluded that the empirical data of the complex dielectric function only accurately represent the bulk properties of the noble metals. Therefore, the bulk dielectric function will not be satisfactory for the description of optical properties of noble nanoparticles, where in general the nanoparticles are comparatively small with respect to the continuous thin films in the Johnson and Christy experiments. In the following sections a theoretical background will be given for the analytical representation of the size-dependent dielectric function.

2.2.2 Drude model and bulk dielectric function

The frequency dependent dielectric function $\tilde{\epsilon}(\omega)$ of a metal describes metal's response to incident electromagnetic waves. The dielectric function of noble metals is governed by interband and conduction band transitions. To some extent, the optical properties of noble nanoparticles can be described as a free electron metal using the Drude-Lorentz-Sommerfeld model [42, 45, 46]. It is assumed that the response of a free electron of mass m_e and charge e to an external electric field $\mathbf{E} = \mathbf{E}_0 \mathrm{e}^{-i\omega t}$ is given by simple equation of motion

$$m_e \frac{d^2\mathbf{r}}{dt^2} + m_e \Gamma \frac{d\mathbf{r}}{dt} = e\mathbf{E}_0 \mathrm{e}^{-i\omega t}, \tag{2.33}$$

where Γ is a phenomenological damping constant, and $\mathbf{r}$ is an electron's displacement. The polarization in this case can be given by $\mathbf{P} = \rho_\mathrm{e}\mathbf{p}$, where ρ_e is electron density and $\mathbf{p} = e\mathbf{r}_0$ is a dipole moment. The polarization $\mathbf{P}$, with assumption of the isotropic medium ($\mathbf{P} \,||\, \mathbf{E}$) [45], related to dielectric function $\tilde{\epsilon}(\omega)$ by the definition (substitution of 2.13 into 2.11) $\tilde{\epsilon} = 1 + \mathbf{P}/(\epsilon_0 \mathbf{E})$. Thus, the frequency-dependent dielectric function $\tilde{\epsilon}(\omega)$ of a system of ρ_e free electrons can be deduced from these equations,

$$\tilde{\epsilon}(\omega) = 1 - \frac{\omega_p^2}{\omega^2 + i\Gamma\omega} = 1 - \frac{\omega_p^2}{\omega^2 + i\Gamma^2} + i\frac{\omega_p^2 \Gamma}{\omega(\omega^2 + \Gamma^2)}, \tag{2.34}$$

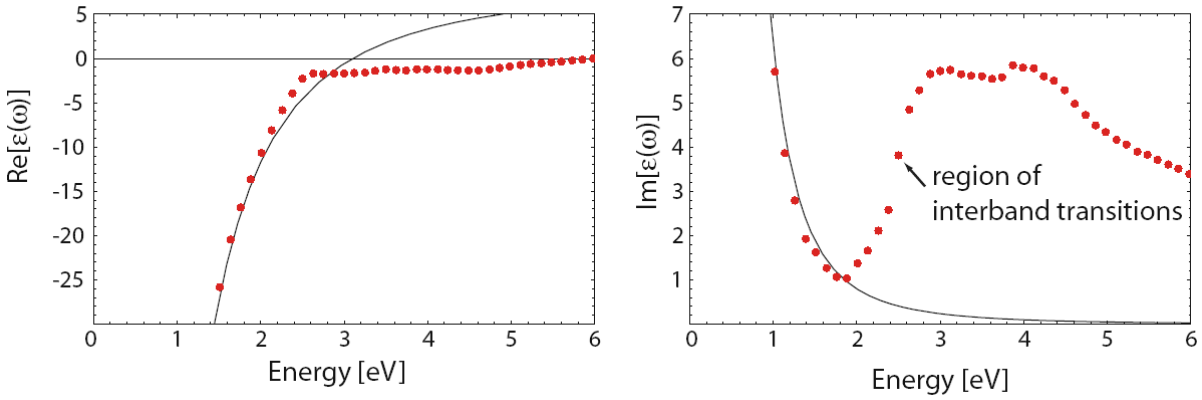

Figure 2.4: Dielectric function $\tilde{\epsilon}(\omega)$ (2.34) of the free electron gas (solid line) fitted to the literature values of the dielectric data for gold [44] (dots). Interband transitions limit the validity of this model at visible and higher frequencies. Reprinted from ref. [42]

where $\omega_p = \sqrt{\frac{\rho_e e^2}{\epsilon_0 m_e}}$ is the plasma frequency[6] of the free electron gas. In this classical model (2.34) the damping constant Γ occurs due to the scattering of the electrons with phonons, electrons, lattice defects and impurities and can be related to mean free path l_∞ of the electron between collisions and the Fermi velocity $v_F = 1.41$ nm/fs by $\Gamma = v_F/l_\infty$ [45].

2.2.3 Interband transitions

In real metals, the validity of free-electron model is limited due to the contribution of both free electrons and interband transitions. In case of the alkali metals, the contribution from the interband transitions can be neglected up to the ultraviolet frequency range. However, interband transitions of the noble metals start to occur in the visible frequency range ($\lambda = 1.77 - 3.1$ eV) and can be seen on the example of the gold dielectric function (Figure 2.4). To incorporate the contribution of interband transitions in the noble metals, the complex dielectric function can be rewritten as a sum of susceptibilities $\tilde{\chi}^{\mathrm{IB}}$ and $\tilde{\chi}^{\mathrm{D}}$, due to interband and free electrons respectively as

$$\tilde{\epsilon}(\omega) = 1 + \tilde{\chi}^{\mathrm{IB}} + \tilde{\chi}^{\mathrm{D}} = 1 - \frac{\omega_p^2}{\omega^2 + i\Gamma\omega} + \tilde{\chi}^{\mathrm{IB}}. \tag{2.35}$$

[6]For gold $\omega_p = 1.38 \cdot 10^{16}$ 1/s [45]

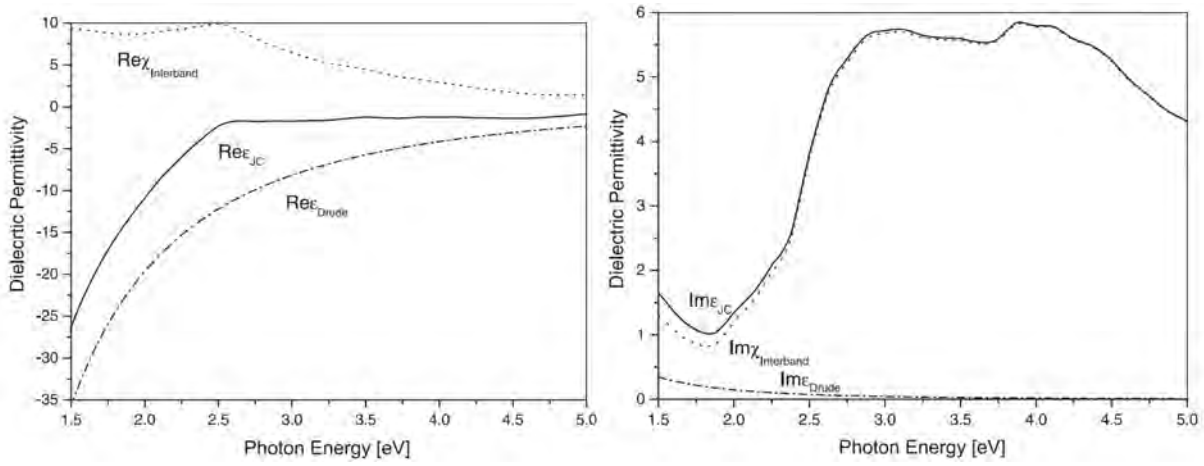

Figure 2.5: Interband and free electron contribution to dielectric function $\tilde{\epsilon}(\omega)$ of bulk gold and experimental values from [44]. Reprinted from ref. [47]

The interband susceptibility $\tilde{\chi}^{\mathrm{IB}}$ leads to a red shift of the resonance frequency, bigger contribution of $\tilde{\chi}^{\mathrm{IB}}$ to overall dielectric function in the visible range (Figure 2.5). It can be seen by decomposition, with the use of (2.35), of the experimental bulk dielectric function of the gold [44] to Drude and interband transition part (see Figure 2.5), where the imaginary part of the interband susceptibility $\Im(\chi^{\mathrm{IB}})$ related to direct energy dissipation and becomes dominant in the region of interband transitions and the real part of the interband susceptibility $\Re(\chi^{\mathrm{IB}})$ also plays an important role in contributions to the dielectric function at smaller frequencies.

2.2.4 Surface scattering - limited mean free path effect

The analytical expression for the bulk dielectric function has been based on solid-state theory. The expression (2.35) is only valid for big clusters (nanoparticles with radius more than 10 nm [45]), where the damping constant ($\Gamma_{\mathrm{bulk}} = v_{\mathrm{F}}/l_{\infty}$) is a sum of contributions due to electron interactions with phonons, electrons, lattice defects and impurities. When the cluster size becomes comparable or smaller than the bulk mean free path l_{∞} of the electrons between collisions, additional scattering of the conduction electrons from the cluster surface occur. The addition of this scattering will shorten the mean free path between collisions, and will increase the damping constant. To introduce corrections for the *intrinsic* effects, due to the bulk dielectric function, the damping constant can be

written as [45],

$$\Gamma = \Gamma_{\text{bulk}} + \Gamma_{\text{surf}} = \gamma_0 + \frac{A v_{\text{F}}}{L_{\text{eff}}}. \tag{2.36}$$

where A is a dimensionless constant ("broadening" parameter) on the order of unity, L_{eff} is the reduced effective mean free path length and γ_0 is the bulk relaxation frequency[7]. For the case of the spherical particles L_{eff} equals to the radius of the sphere with an equivalent volume ($L_{\text{eff}} = R = \sqrt[3]{\frac{3V}{4\pi}}$). In the case of the arbitrary shaped object, Coronado *et. al.* [48], in their calculations of the effective electron mean free path, in comparison of the classical approach (2.36) against quantum box models, obtained better results with $L_{\text{eff}} = \frac{4V}{\text{S}}$, where V is the volume and S is the surface area of the object.

2.2.5 Radiation damping

Radiation damping Γ_{rad} is another dephasing process that can contribute to the overall *intrinsic* retardation effects. As it was shown by Sönnichsen [49, 50, 38] (Figure 2.6), the radiation damping is sensitive to the particle volume, and rapidly increases the damping constant Γ for gold spheres wider than 40 nm in diameter. In his calculations Sönnichsen [49] used an empirical equation to compute the non-radiative damping:

$$\Gamma_{\text{nonrad}} = 77 + \text{e}^{(\text{E}_{\text{res}} - 1.334)/0.171}, \tag{2.37}$$

where Γ_{nonrad} is given in the units of meV and E_{res} is a resonance energy of the measured particle is in the units of eV. Radiative damping Γ_{rad} was calculated as a difference between total measured damping Γ and the combination of non-radiative dampings

$$\Gamma_{\text{rad}} = \Gamma - \Gamma_{\text{nonrad}}. \tag{2.38}$$

The Figure 2.6 shows that the radiative damping plays important role for gold nanospheres with diameters between 40 and 150 nm and shouldn't be neglected in size corrections to bulk dielectric function.

Novo *et. al.* [39] investigated longitudinal resonance broadening and significance of radiation damping for gold nanorods of different aspect ratio and size. In their experiments (Figure 2.7), Novo *et. al.* [39] compared contributions of all retardation ef-

[7]For gold $\gamma_0 = 1.094 \cdot 10^{14}$ 1/s [44]

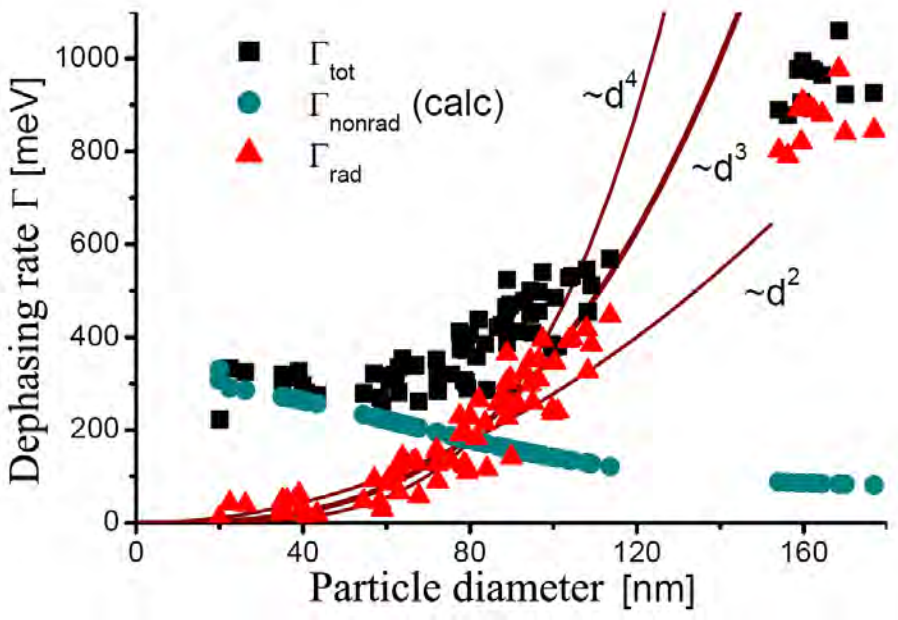

Figure 2.6: Dephasing rates in gold nanospheres as function of diameter. Γ_{tot}: measured, Γ_{nonrad}: calculated by Eqn. 2.37, Γ_{rad}: calculated by subtracting the two. Reprinted from ref. [49].

fects to the damping constant Γ where, based on the dipole approximation, radiation damping was proportional to the particle volume and was given by $\Gamma_{\text{rad}} = \frac{\hbar \eta V}{\pi}$, with $\eta = (5.5 \pm 1,5) \times 10^{-7}$ fs^{-1}nm^{-3} (averaged based on several experimental data of Novo *et. al.* [39] and Sönnichsen *et. al.* [38]).

$$\Gamma = \Gamma_{\text{bulk}} + \Gamma_{\text{surf}} + \Gamma_{\text{rad}}. \tag{2.39}$$

As it can be seen from Figure 2.7 (red line, where $\Gamma = \Gamma_{\text{bulk}} + \Gamma_{\text{surf}} + \Gamma_{\text{rad}}$), the contribution of all three damping processes (2.39) gives satisfactory agreement with experimental data of Novo *et. al.* Figure 2.7 (dotted line, where $\Gamma = \Gamma_{\text{bulk}} + \Gamma_{\text{rad}}$) also shows that radiation damping starts to play a significant role for gold nanorods wider than $\sim$ 20 nm in effective mean free path L_{eff}. For narrower nanorods the broadening of the resonance comes from the surface scattering (dashed line in the Figure 2.7, where $\Gamma = \Gamma_{\text{bulk}} + \Gamma_{\text{surf}}$).

In this thesis, the optical properties of gold nanorods with an effective mean free

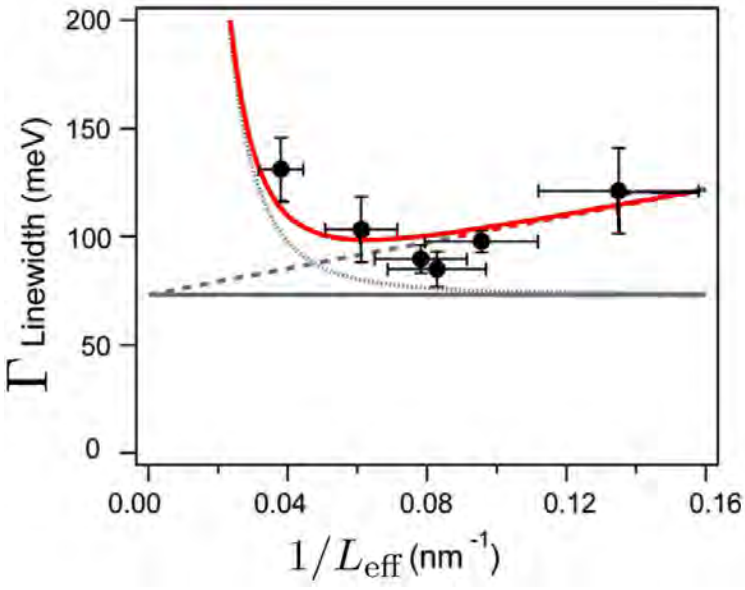

Figure 2.7: Damping constant Γ versus $1/L_{\text{eff}}$ for gold nanorods with aspect ratios between 2 and 4. The error bars indicate the standard deviations. The lines show calculated dampings from bulk scattering (Γ_{bulk}, horizontal line), bulk plus surface scattering ($\Gamma_{\text{bulk}} + \Gamma_{\text{surf}}$, dashed line), and bulk plus radiation damping ($\Gamma_{\text{bulk}} + \Gamma_{\text{rad}}$, dotted line). The solid red line shows the total damping Γ. Reprinted from ref. [39].

path length L_{eff} ranging from 7.5 to 8.2 nm were considered, which corresponds to the inverse effective path length ($1/L_{\text{eff}}$) of 0.12 - 0.13 nm^{-1} (Figure 2.7). For these nanorods, radiation damping is negligible and can be omitted from retardation effects, leaving (2.36) as an appropriate representation of the damping in size dependent dielectric function of gold.

2.3 Dielectric function: summary

For gold nanoparticles with a diameter less than 40 nm nonradiative damping dominates. The complex dielectric is than given by

$$\tilde{\epsilon}(\omega, L_{\text{eff}}) = \tilde{\epsilon}_{\text{bulk}} + \frac{\omega_p^2}{\omega^2 + i\omega\gamma_0} - \frac{\omega_p^2}{\omega^2 + i\omega\left(\gamma_0 + \frac{Av_{\text{F}}}{L_{\text{eff}}}\right)}, \tag{2.40}$$

where $\tilde{\epsilon}_{\text{bulk}}$ accounts for the interband transitions and $\frac{Av_{\text{F}}}{L_{\text{eff}}}$ includes the limited mean free path effect to the bulk dielectric function. For gold nanoparticles with diameters ranging from 40 to 150 nm, radiative damping dominates. In this case, the complex dielectric function of gold is

$$\tilde{\epsilon}(\omega, L_{\text{eff}}) = \tilde{\epsilon}_{\text{bulk}} + \frac{\omega_p^2}{\omega^2 + i\omega\gamma_0} - \frac{\omega_p^2}{\omega^2 + i\omega\left(\gamma_0 + \frac{Av_{\text{F}}}{L_{\text{eff}}} + \frac{\eta V}{\pi}\right)}. \tag{2.41}$$

For gold nanoparticles with bigger diameters, the dielectric function will take a form of a bulk dielectric function ($\tilde{\epsilon}(\omega, R) = \tilde{\epsilon}_{\text{bulk}}$) and can be represented by experimental data of Johnson and Christy [44].

2.4 The finite element method

As mentioned in the previous chapter the finite element method is a numerical technique that finds an approximate solution to a partial differential equation by decomposing it into a system of simpler equations. This method is widely used today to describe the behavior of an electromagnetic wave incident on an object with dielectric properties different from a surrounding medium. In FEM it is realized by solving the Maxwell's equations (2.1-2.4) as a system with complex boundary conditions. To demonstrate the method, consider a homogeneous spatial domain Ω, where time-harmonic electric field defined by the Helmholtz wave equation (2.18). This is a typical boundary-value problem that has a form

$$\mathfrak{L}\phi = f = 0, \tag{2.42}$$

where $\mathfrak{L} = (\nabla \times \nabla \times -\kappa_0^2\tilde{\epsilon})$ is a differential operator, $\phi = \mathbf{E}$ is an unknown function to be computed in the region Ω and f is a forcing term(or excitation). Boundary conditions that enclose domain Ω can be as simple as Neumann ($\mathbf{n} \cdot \nabla\phi = S$, where $\mathbf{n}$ is a normal vector and S is a scalar function) or Dirichlet conditions ($\phi = S$), or more complex impedance and radiation conditions. The computational domain Ω is divided into smaller elements, Ω_e, size of which depends on expected variations of the unknown function. The solution for the unknown function ϕ within each element, is approximated by an expansion with a finite number of basis functions, $\acute{\phi} \approx \sum_{i=1}^{N} c_i v_i$, where c_i are unknown coefficients of the

basis functions v_i. The solution in this system of N equations, produces $\acute{\phi}$ that is a best fit to the unknown function ϕ. Variational formulation and weighted residual formulation are two well known methods to solve this problem and find coefficients.

The variational method [35, 36, 37], also known as Ritz method, is based on formulating the boundary-value problem (2.42) in terms of a functional. It can be shown that for the case of a self-adjoint and positive-definite operator $\mathfrak{L}$, the functional can be written in the form

$$F_e(\acute{\phi}) = \frac{1}{2}\int_{\Omega_e} \acute{\phi}\mathfrak{L}\acute{\phi}d\Omega - \int_{\Omega_e} f\acute{\phi}d\Omega. \tag{2.43}$$

The minimization of the function $F_e(\acute{\phi})$, produces coefficients c_i so $\acute{\phi}$ is the best approximation to the solution.

The weighted residual method [35, 36, 37], is another way to find an approximate solution to (2.42). If a trial function $\acute{\phi}$ is an approximate solution to (2.42), then substitution of it into ϕ will yield a nonzero residual $r = \mathfrak{L}\acute{\phi} - f \neq 0$. In order to obtain the best approximation of $\acute{\phi}$, residual r must be as small as possible at all locations in Ω_e. To force this condition, test or weighting functions w_i (where i is the number of unknown degrees of freedom in the approximation), need to be chosen so weighted residual integrals R_i

$$R_e = \int_{\Omega_e} w_i r d\Omega = 0. \tag{2.44}$$

The guess coefficients will determine the accuracy of found approximate solution to the (2.42) within Ω_e. To summarize FEM, in order to solve problems defined by PDEs, the following steps should be taken: a) discretize the computational domain Ω into smaller elements (triangle or tetrahedral for 2D and 3D space); b) define an interpolation function; c) for the element, assemble the system of equations by the use of Ritz or weighted residual method; d) and solve the equations.

In this thesis a commercially available finite element based software called COMSOL Multiphysics © 3.5a (COMSOL AB, Stockholm) was used to develop a numerical model that will be described in the following subsections.

Chapter 3

Methods

In this chapter numerical and experimental methods for single gold nanoparticle characterization will be given. It will start with a brief description of the finite element model and continue with a description of an experimental validation technique that was used for the numerical model validation.

3.1 The computational model

In electromagnetic problems, when it is needed to determine the propagation of an electromagnetic wave in anisotropic or layered media, a full field formulation for the finite element modeling should be used. In the full field formulation the incident electric field [35, 37] usually defined by an analytical expression for the plane wave, $\mathbf{E}_{\text{inc}} = \mathbf{E}_0 \mathrm{e}^{-j\kappa z}$, where κ is a wavenumber and $\mathbf{E}_0$ is the amplitude of the incident electric field. The electric field wave propagation is found by solving the Helmholtz wave equation (2.18) for the total electric field. The scattered component of the electric field can be calculated as a difference between the total and incident electric fields, $\mathbf{E}_{\text{scat}} = \mathbf{E}_{\text{total}} - \mathbf{E}_{\text{inc}}$.

The full field formulation was used to simulate the experimental setup of Spatial Modulation Spectroscopy (SMS) [40, 41, 51, 52] technique, which was used to obtain experimental optical properties of the single gold nanorod and validate size corrections for bulk dielectric function of gold (see section 3.2 for a description of this technique). A schematic illustration of the model's geometry is shown in the Figure 3.1. The computational domain was subdivided with the following regions: GNR with silica shell on

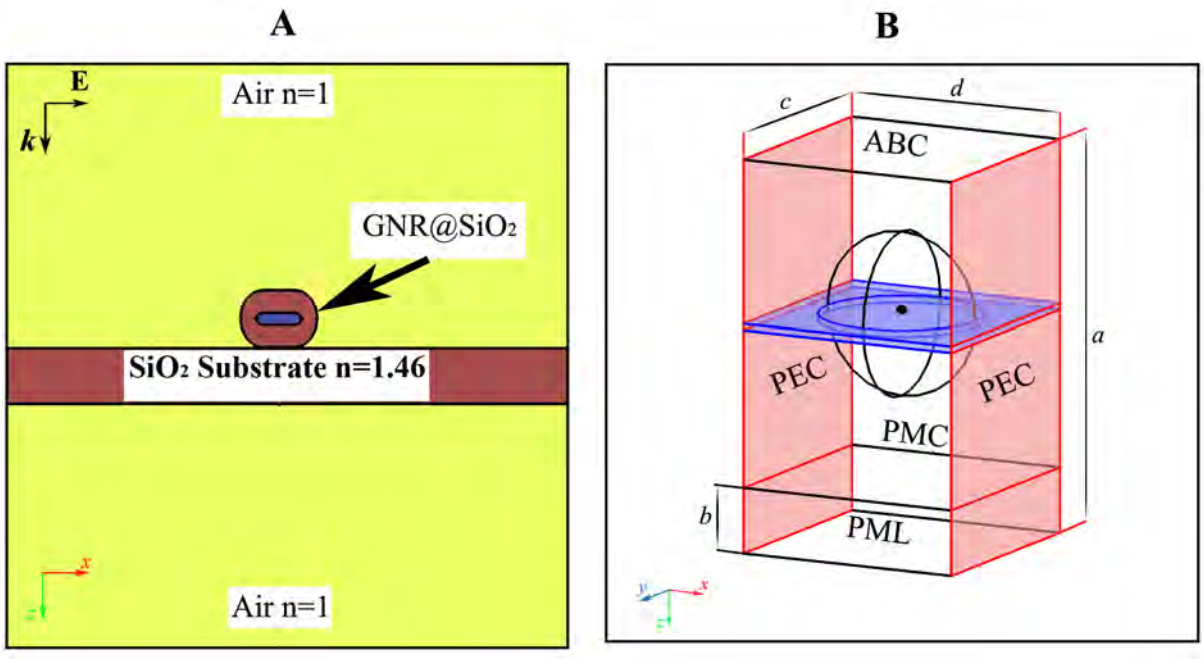

Figure 3.1: (A) Schematic of single nanorod on top of a 40 nm thick substrate layer model. (B) Geometry and boundary conditions of the computational model. Dimensions: $a = 2.4$ μm, $b = 0.4$ μm, $c = d = 1.4$ μm.

top of a silica substrate layer, air domains above and below the substrate and a perfect matched layer (PML) at the bottom that absorbs the normal component of any incident wave.

The incident electric field originated at the top boundary and propagates in the positive z-direction with a polarization along longitudinal axis of the nanorod (see Figure 3.1). The top and the bottom boundaries are also defined as a absorbing boundary condition (ABC) which is also known as Sommerfeld radiation condition [35, 37]. The ABC was defined so that the boundary appears transparent to the incident radiation and absorbs the scattered field in all directions. In order to truncate the size of the computation domain on the sides, perfect electric conductor (PEC), $\mathbf{n} \times \mathbf{E} = \mathbf{0}$, and perfect magnetic conductor (PMC), $\mathbf{n} \times \mathbf{H} = \mathbf{0}$, conditions were used at the boundaries parallel and perpendicular to the incident electric field polarization, respectively. All others internal boundaries had the field continuity condition, given by (2.19-2.22).

The dimensions of the computational domain (see Figure 3.1) were chosen so that

any further increase in the domain size will not affect the solution. The substrate layer thickness was equal 40 nm which corresponds to the actual thickness of the TEM grid film in the SMS setup.

The meshing quality of the computational domain plays an important role in FEM. In order to obtain the correct solution, at least 10 linear elements per wavelength were used during meshing of the geometries with even more fine refinement of the nanoparticle's mesh.

3.1.1 The Mie solution

The Mie solution is an analytical solution of Maxwell's equations for the incident plane electromagnetic waves on a spherical object with a radius on the order of a wavelength [53].

To test finite element model against the Mie solution, the regions of the computational domain were represented as a homogeneous medium with refractive index, $n = 1.45$, (which is equal to the averaged refractive index of silica). A gold sphere with 10 nm radius and bulk dielectric function of gold [44] was inserted into computational domain, leaving the boundary conditions the same as described above. An additional spherical boundary with the radius of 540 nm (see Figure 3.1) was placed around the gold sphere for near the field calculations (2.28).

The Mie solution for the gold sphere with the same parameters as of FEM model was obtained with the use of SigmaMie 1.05 code of P. Maioli [54].

3.2 Experimental validations

In the following sections two types of the experimental validations are presented. In the first one the model's sensitivity was tested against spectrophotometry measurements of the uncoated and coated gold nanorods in the colloidal solution. In the second one an overview of Spatial Modulation Spectroscopy with TEM correlation is given. At the end, modeling of the single gold nanorod's optical response is presented.

3.2.1 Uncoated and coated colloidal GNRs

The sensitivity of the computational model to the changes in the surrounding environment was tested using the prediction of the resonance peak position shift due to the coating of gold nanorods with silica. The test was done by a comparison of an extinction cross-section from the silica coated and uncoated gold nanorod simulations with an experimental data of spectrophotometry on a colloidal solution of coated and uncoated gold nanorods.

Gold nanorods were prepared and silica coated by Maria F. Cardinal (Unidad Asociada CSIC-Universidade de Vigo), as described by [55]. TEM imaging of the same colloidal solution of GNRs, before and after silica coating, was done to obtain the statistical distribution of nanorod size and silica shell thickness (see Figure 3.2). Figure 3.3

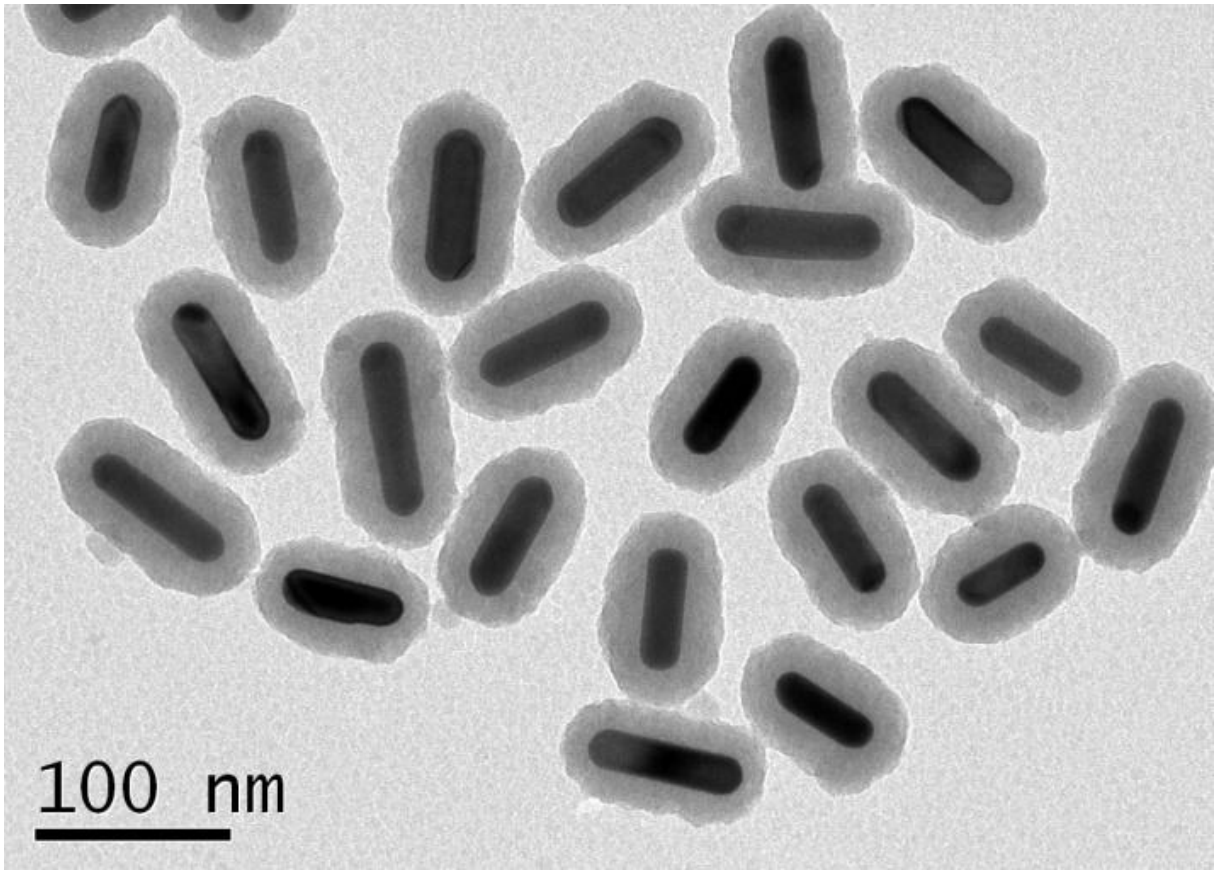

Figure 3.2: TEM image of coated GNRs.

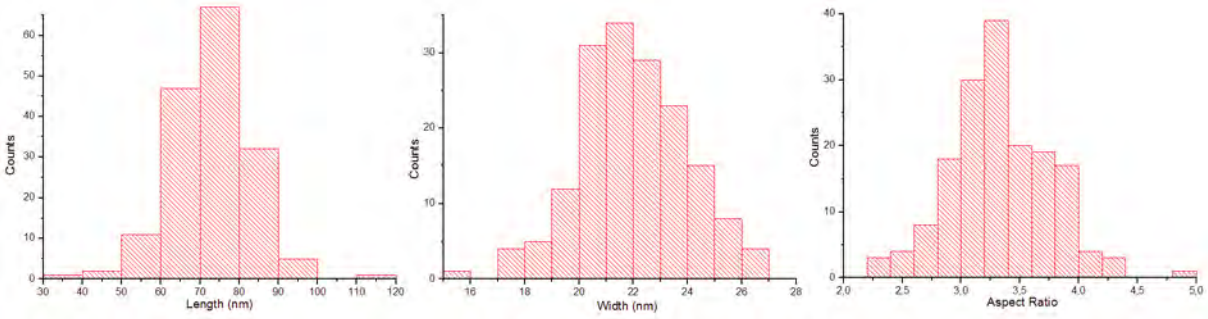

Figure 3.3: Histograms of GNR's dimensions distribution.

shows the statistical distribution of gold nanorod size, measured with TEM. The sampled population of nanorods had a mean/standard deviation for the length of 72.88/10.22 nm, for the width of 21.93/2.0 nm and for the aspect ratio of 3.33/0.43.

The standard deviation of the length and width of the GNRs, influence the FWHM and the magnitude of the absorption peak, while the peak position is determined solely by the aspect ratio of the nanorods (assuming the same surrounding and the same end-tip shape for all nanorods). The influence of the interband transitions of the gold on the resonance peak position was accounted using the experimental values of bulk dielectric function of gold [44].

As mentioned earlier, the absorption spectrum of a GNR has two peaks corresponding to parallel and perpendicular polarization of the light with respect to the longest axis of the rod. The GNRs were orient randomly in a colloidal solution used for spectrophotometer measurements. In order to mimic this random orientation of GNRs in the computational model, the average weighted extinction cross-sections from two orientations, longitudinal and transverse was calculated (for details see [18]). As it was shown by Cole *et. al.* [18], the average weighted extinction of randomly oriented nanorods is calculated as a sum of the extinction cross-sections, $\frac{2}{3}\sigma_{\text{ext}}$ and $\frac{1}{3}\sigma_{\text{ext}}$, associated with a transverse and longitudinal polarization of the light with respect to the nanorod's longest axis, respectively. The far-field scattering cross-section calculations was done with the use of the Stratton-Chu formulas [56, 57].

Since the main purpose of this experimental validation was to determine whether the computational model can accurately predict the positions of the absorption peaks of the gold nanorod solution, the mean GNR size, based on the statistical distribution (see

Figure 3.3) was simulated with the shape of a cylinder with hemi-spherical end-tips and embedded in homogeneous medium of water ($n = 1.33$).

Based on the statistics from the TEM measurements, the mean/standard deviation of the silica thickness in the middle of the rod on average were a 18.5/1.6 nm and at the rod end-tip it was 15.6/1.5 nm. Similar to the previous simulations, a GNR of the same size embedded in a silica ($n = 1.46$) shell with an average thickness that corresponded to TEM measurements and surrounded by homogeneous medium of water ($n = 1.33$) was simulated.

3.2.2 Single GNR measurement using spatial modulation spectroscopy

Several spectroscopic techniques are currently available [50, 52, 58, 59] for the detection and optical characterization of individual nanoparticles. Spatial Modulation Spectroscopy (SMS) [40, 41, 51, 52] is a far-field technique that provides a quantitative de-

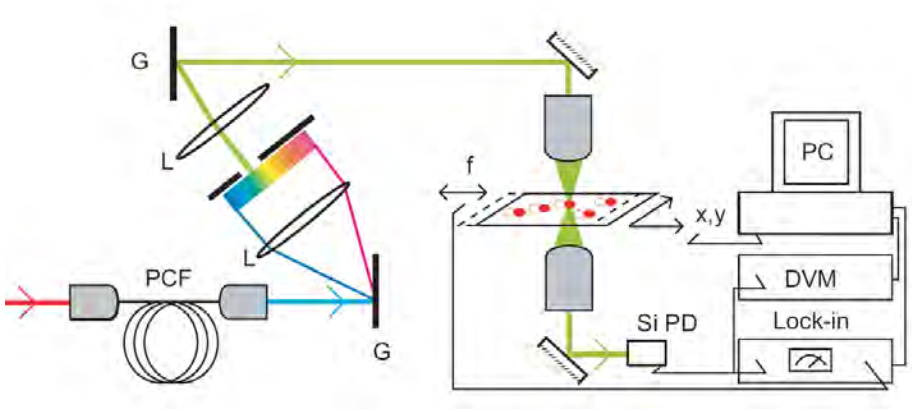

Figure 3.4: Single particle space modulation spectroscopy setup. The space modulation microscope is shown on the right part of the figure, with the two ×100 microscope objectives and the acquisition system (a silicon photodiode (PD), lock-in amplifier, digital voltmeter (DVM) and personal computer). The sample position is modulated along the y direction at the frequency f by a piezo-electric element and displaced by a x, y piezo-scanner. The light source for gold experiments is created by injecting femtosecond pulses in a photonic crystal fiber (PCF), dispersing the created supercontinuum in a grating pair system (G), the part of the supercontinuum selected by a slit being injected in the transmission microscope. Reprinted from ref. [51]

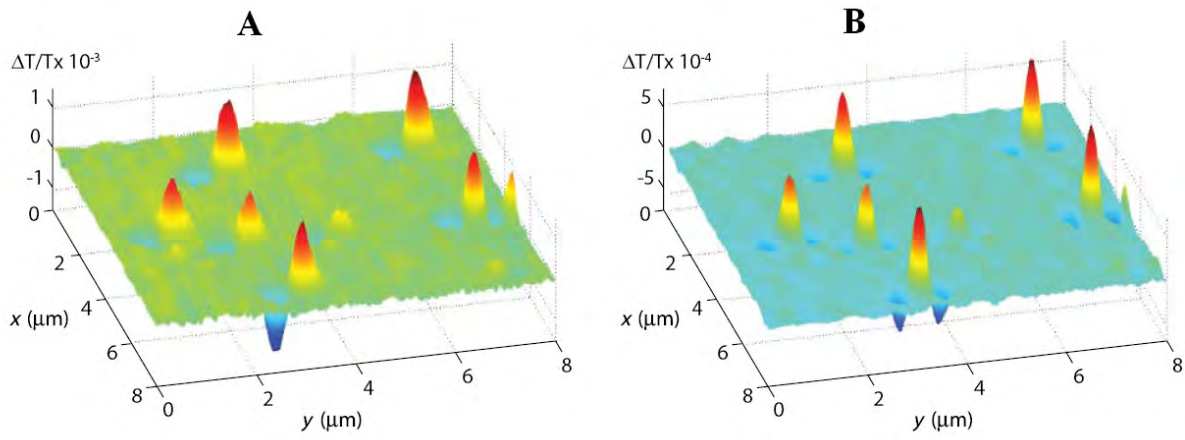

Figure 3.5: Spatial x, y dependence of the transmission change ΔT/T detected at f (A) and $2f$ (B). Each structure corresponds to a single gold nanoparticle, lying in between the two-extrema and at the peak maximum for f and $2f$ detection, respectively (the mean particle diameter is D $\approx$ 20 nm). The laser, with wavelength $\lambda = 532$ nm and power $P_i = 10\mu$W, is focused on a d = 0.34 μm focal spot. For all images, the sample position is scanned over the same 8×8 μm^2 zone and modulated along the y axis at $f = 1.5$ kHz with $\delta \approx 0.3$ μm. Reprinted from ref. [60].

termination of the extinction cross-section of a single nanoparticle. SMS is based on modulation of the particle's spatial position in the focal spot of a tightly focused laser beam. It is applicable for small nanoparticles where absorption dominates over scattering. The changes in the transmitted power due to spatial modulation of position (Figure 3.4) can be detected and directly related to the nanoparticle extinction cross-section.

During SMS modulation the transmitted laser power P_t is measured. From this the extinction cross-section of the particle can be obtained,

$$P_\mathrm{t}(x, y) \approx P_\mathrm{i} - \sigma_\mathrm{ext} I(x, y) \tag{3.1}$$

where the intensity spatial profile, $I(x, y)$, of the focal spot and incident laser power P_i are known, while σ_ext is the extinction cross-section of the particle in the focal spot. Scanning the focal plane of the nanoparticle position at a modulation frequency, f, or a harmonic frequency, $2f$, will produce a profile proportional to the first or second derivative of the laser beam intensity $I(x, y)$ [40, 41, 51, 52], respectively (Figure 3.5). The amplitude of the modulated signal is proportional to the extinction cross-section σ_ext of the imaged

particle,

$$\Delta T/T = \frac{P_{\mathrm{i}} - P_{\mathrm{t}}}{P_{\mathrm{i}}} = -\frac{\sigma_{\mathrm{ext}} I(x,y)}{P_{\mathrm{i}}}, \tag{3.2}$$

where $\Delta T/T$ is the light transmission change due to the absorption of the light by the imaged particle.

Thus, the extinction cross-section of a single nanoparticle can be directly measured if the laser beam profile and the amplitude of the modulation signal are known.

The SMS experimental setup is also referred as the SMS nanoscope, since it is possible to see the position of the nanoparticle (Figure 3.5). The full details of the SMS technique is produced elsewhere [40, 41, 51, 52].

3.2.3 TEM correlation of single GNRs

The sample preparation for single nanoparticle characterization using SMS consists of spin coating a dilute colloidal solution of gold nanorods onto a transmission electron microscopy (TEM) grid. The used TEM grid has 50×50 μm windows each supported by a 40 nm thin silicon dioxide (SiO_2) film (Figure 3.6 A).

The solution of colloidal gold nanorods needed to be sufficiently diluted to ensure separation of 1 μm between individual nanorods to eliminate any coupling effects between them. A typical scanning signal of a single 50×50 μm window obtained with SMS

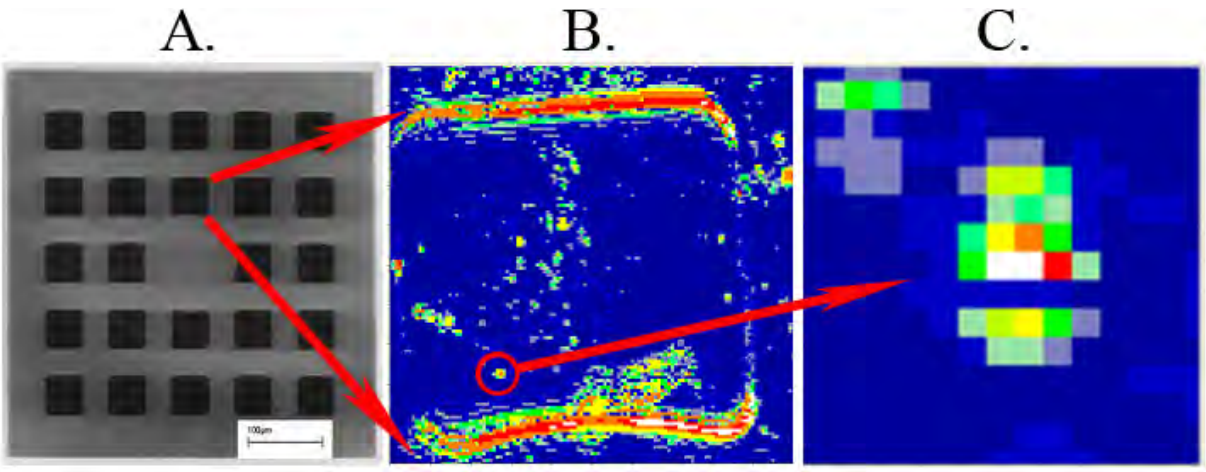

Figure 3.6: (A)TEM grid with 50×50 μm windows, (B) an image of TEM window from SMS nanoscope, (C) a zoom-in view (3×3 μm window) of a gold nanorod from the SMS nanoscope.

nanoscope is shown at Figure 3.6 (B). After locating the signal from a possible nanoparticle, a higher resolution spectrum was obtained (see Figure 3.6 C) and the approximate location of the particle was marked for the follow-up TEM characterization of the particle geometry and dimensions.

3.3 Single GNR validation

For the experimental validation of the size corrected dielectric function of gold (using equation (2.36)), four gold nanorods with a SiO_2 shell (Figure 3.7) were imaged using the SMS at the FemtoNanoOptics group, Université Claude Bernard Lyon 1. As it is shown in the TEM images (Figure 3.7), two different TEM cameras (Camera 1 and Camera 2) were used for the TEM measurements of the nanorods. Furthermore, the size measurement of the GNR_2 was done at 110k magnification, while other nanorods were imaged at 83k magnification. There was a 12% difference in estimated size at 83k magnification between Camera 1 and Camera 2. This difference in measurement is believed to be due to the fact that Camera 2 was not calibrated for an extended period of time, on the other hand Camera 1 was maintained well and calibrated regularly. For that reason gold nanorod GNR_3 that was imaged with TEM Camera 2, was scaled down by 12% of its initialy TEM measured dimensions.

Table 3.1 shows the percentage uncertainty δ in the measurements of the GNRs length (δ_{L}), width (δ_{W}) and aspect ratio (δ_{AR}) from the TEM images (Figure 3.7). The uncertainty was determined using

$$\delta = \frac{|x_{\min} - x_{\max}|}{\frac{1}{2}(x_{\min} + x_{\max})} \times 100\%, \tag{3.3}$$

where $x_{\max}$ and $x_{\min}$ are the highest and lowest value of the size parameter (length, width aspect ratio) estimated from the TEM image.

The quality of the TEM images in Figure 3.7 result in uncertainty of up to 30%.

The GNRs in the model were placed on top of the 40 nm thick silica substrate. The size of the GNRs was given the same as the *measured* dimensions in the TEM measurements (see Table 4.1). All gold nanorods, except GNR_1, in the computational models had a cylindrical shape with a hemi-spherical end-tips. The GNR_1, based on the

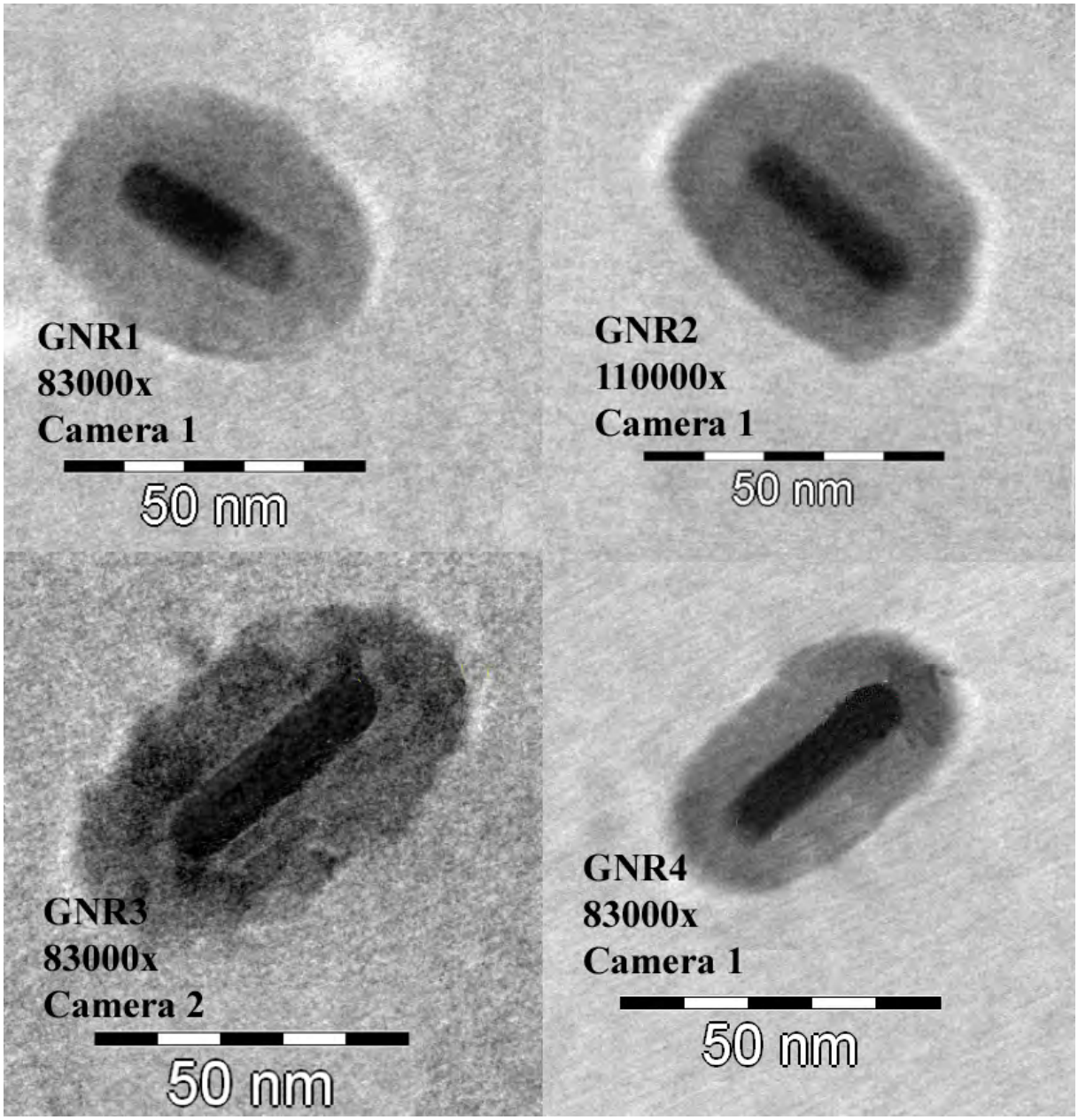

Figure 3.7: TEM images of a single gold nanorods coated with silica shells

TEM camera (magnification)	GNR name	δ_L	δ_W	δ_{AR}
Camera 1 (83k)	GNR_1	5.83%	33.35%	27.70%
Camera 1 (110k)	GNR_2	9.69%	18.85%	30.31%
Camera 2 (83k)	GNR_3	6.06%	4.58%	15.30%
Camera 1 (83k)	GNR_4	10.99%	23.3%	34.10%

Table 3.1: Measurement uncertainty. δ_L, δ_W and δ_{AR} is the percentage difference of TEM measurements of a length, width and aspect ratio, respectively.

TEM characterization, was modeled as a cylinder with much flatter end-tips than a hemisphere. The refractive index of the gold nanorod's silica shell and the TEM substrate were set to a constant value of $n = 1.46$. In the models, the bulk dielectric function of gold was corrected to account for *intrinsic* size effects (see equation 2.40) with parameters given in the Table 4.1 of the results chapter.

In modeling the optical response of a single gold nanorod an assumption was made about the extinction cross-section. As was shown in the section above, in SMS, the scattering from the substrate is subtracted during modulation of the particle position, and the experimental extinction cross-section includes only absorption and far-field scattering cross-sections from the imaged nanoparticle. For nanorods, due to its small size, the scattering cross-section is negligible and can be omitted, so that $\sigma_{ext} \approx \sigma_{abs}$. To test this assumption and determine the contribution of absorption and far-field scattering cross-sections to extinction, the gold nanorod GNR_2 was modeled in a vacuum. The result of this simulation is given in the section 4.2.

3.4 Adjusting of the GNR's size in a single nanorod modeling to fit experimental data

As a first step in a single gold nanorod modeling, all nanorods were modeled with sizes measured during TEM imaging (Table 4.1).

Due to the size uncertainties associated with TEM characterization of the imaged nanorods (see Table 3.1), the dimensions of a single gold nanorod in the computational model was subsequently altered to fit an experimental extinction spectrum of the SMS measurements. The fitting was done as follows:

1. Decrease the GNR's volume (while maintaining its aspect ratio) until the magnitude of the extinction peak matches the experimental peak.

2. Adjust broadening parameter A of the size-corrected dielectric function of gold until the FWHM matches the experimental spectrum.

3. Change aspect ratio of the rod (while maintaining its volume), to fit the extinction peak position of the experimental data.

Chapter 4

Results

The finite element model was tested against an analytical solution of Maxwell's equations to validate the finite element method as an appropriate method to model plasmonic nanoparticles. The sensitivity of the computational model to a changes in a dielectric surrounding of a gold nanorod was validated against the spectrophotometer measurements of a colloidal GNR solution. Furthermore, to validate the input parameters of the dielectric function of gold, the finite element method predictions were compared against experimental data.

4.1 Finite element model validation against analytical solution

A finite element model of a gold sphere with 10 nm radius and bulk dielectric constants of gold [44] surrounded by dielectric environment with refractive index $n = 1.45$ (Figure 3.1), was compared against the Mie solution with the same parameters. A comparison of the computational model results and analytical solution is shown in Figure 4.1.

The extinction cross-section from FEM solution very closely matches the analytical solution, having the same position of the extinction peak and full width half maximum (FWHM) of the spectrum, which corresponds to the main parameters in the characterization of the nanoparticle's optical properties.

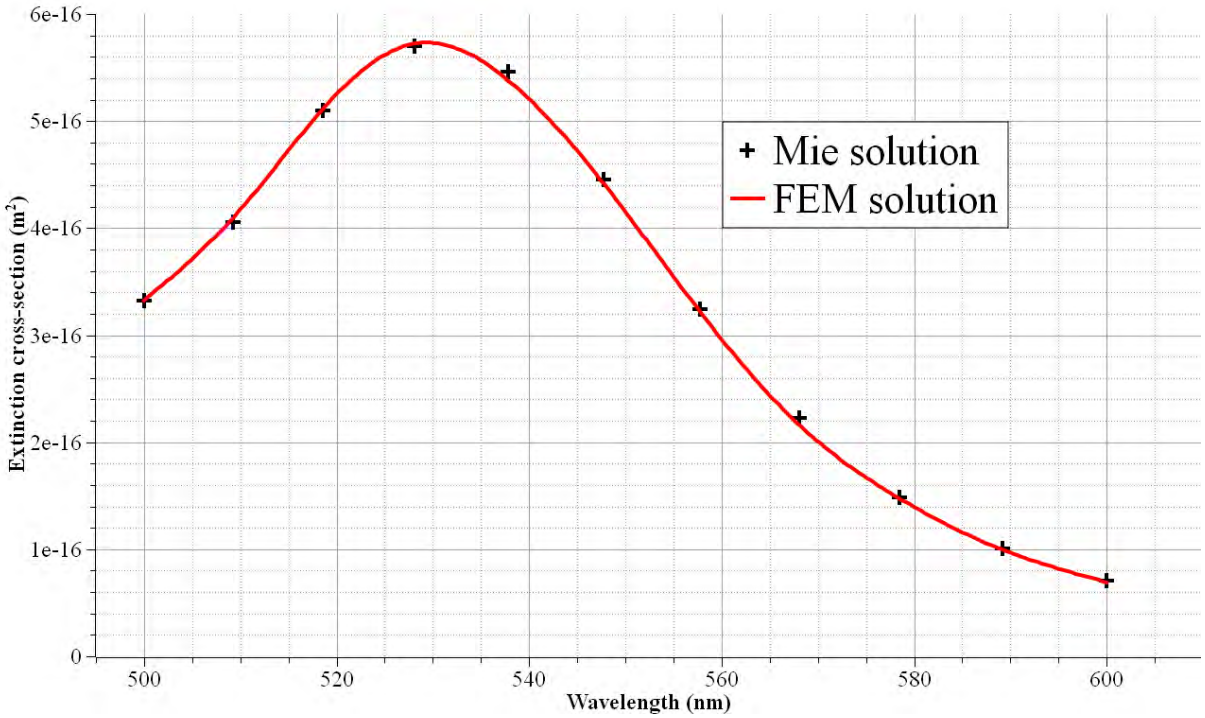

Figure 4.1: Comparison of extinction cross-section from the finite element (COMSOL) model and Mie solution for a gold sphere with radius of 10 nm and bulk dielectric function of gold.

4.2 Finite element model validation against spectrophotometer measurements

For experimental validation, predictions from the computational model were compared against spectrophotometer measurements of a gold nanorod colloidal solution before and after coating with silica.

The Figure 4.2 (A) shows a comparison of average weighted extinction spectrum (normalized to the longitudinal peak height) of a GNR modeled in a homogeneous medium with index of refraction of water ($n = 1.33$) and bulk dielectric function of gold [44] against experimental measurements from spectrophotometry. As shown in the Figure 4.2 (A), the computational model accurately predicts the transverse and longitudinal resonance peak position. Differences in the experimental and numerical FWHM correspond to the size and orientation distributions of the gold nanorods in a colloidal solution (see Figure 3.3).

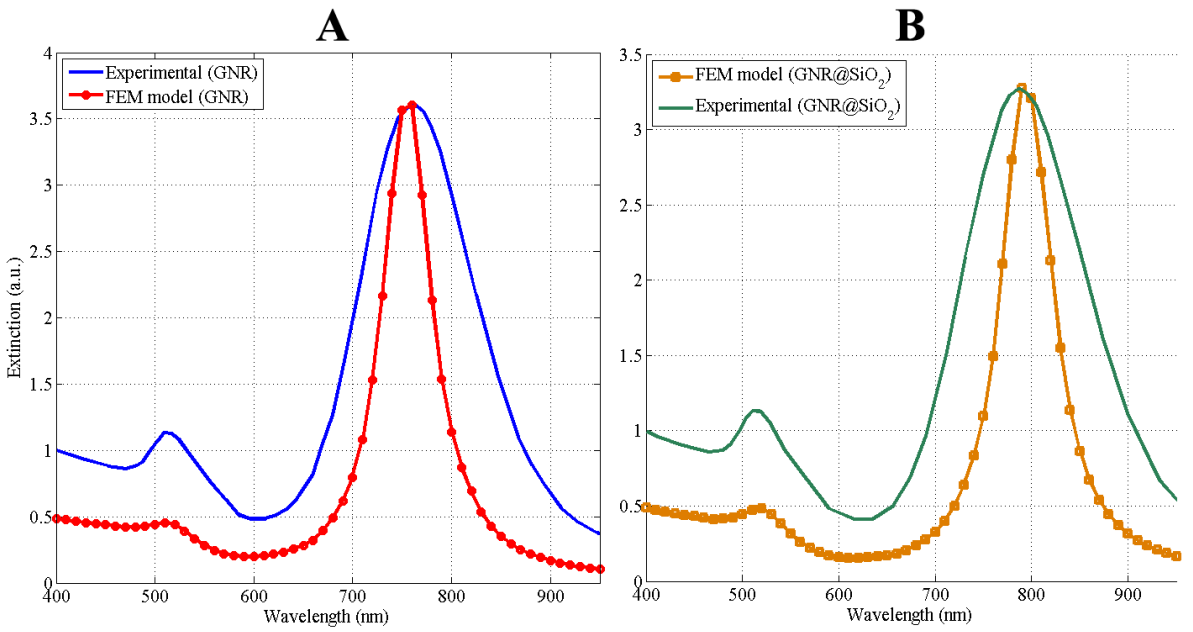

Figure 4.2: Experimental extinction spectra of a colloidal solution compared to numerical simulated spectrum of a single GNR (dimensions 72.88 × 21.93 nm) (A) before coating and (B) after coating with a silica thickness of 18.5 nm in the middle and 15.6 nm at the rod tip. Simulated spectrum of a single GNR normalized to the longitudinal peak height of the experimental spectrum.

Similar to the previous simulations, a GNR of the same size embedded in a silica ($n = 1.46$) shell with an average thickness corresponded to TEM measurements and surrounded by homogeneous medium of water ($n = 1.33$) was simulated. A comparison of the normalized average weighted extinction spectra from the computational model and experimental spectrum is shown in the Figure 4.2 (B). The finite element model accurately predicts the shift in the longitudinal peak position due to silica coating.

4.3 Finite element model validation against single gold nanorod measurements

The assumption that $\sigma_{\text{ext}} \approx \sigma_{\text{abs}}$ was made when modeling the optical response of a single gold nanorod (see section 3.3). This assumption was tested by modeling the

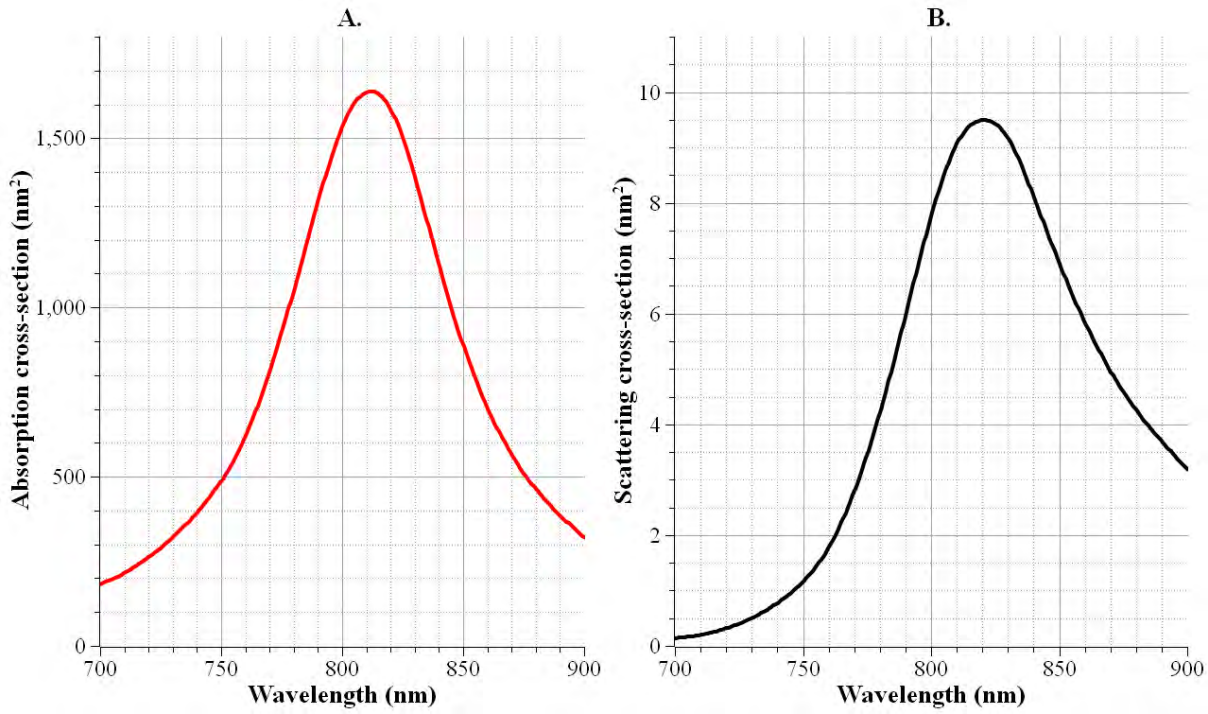

Figure 4.3: Comparison of contribution to extinction cross-section from absorption (A) and scattering cross-section (B) of GNR_2 nanorod in a vacuum.

GNR_2 with parameters from the Table 4.1, in the homogeneous environment of vacuum. Calculated absorption and far-field scattering cross-sections are shown in the Figure 4.3. Comparison of the absorption ($\sigma_{\text{abs}} = 1645$ nm^2) and far-field scattering ($\sigma_{\text{sca}} = 9.5$ nm^2) cross-sections peak amplitude, shows that the scattering is negligible (adds less than 1% to total extinction) and extinction $\sigma_{\text{ext}} \approx \sigma_{\text{abs}}$.

In the Table 4.1 the dimensions of a single gold nanorod used in simulations are given with a percentage error e between the measured and fitted parameters of the nanorod. The percent error was calculated as

$$e_L = \frac{L_r(fitted) - L_r(measured)}{L_r(measured)} \times 100\%, \tag{4.1}$$

$$e_{\text{W}} = \frac{W_r(fitted) - W_r(measured)}{W_r(measured)} \times 100\%, \tag{4.2}$$

and

$$e_{\mathrm{AR}} = \frac{AR_r(fitted) - AR_r(measured)}{AR_r(measured)} \times 100\%. \tag{4.3}$$

Name	$L_{\mathrm{r}}\left[\frac{m}{f}\right]$(nm)	e_{L}	$W_{\mathrm{r}}\left[\frac{m}{f}\right]$(nm)	e_{W}	$AR_{\mathrm{r}}\left[\frac{m}{f}\right]$	e_{AR}	L_{tip}(nm)	L_{mid}(nm)
GNR_1	33.33 30.39	−8.8%	10.15 8.98	−11.5%	3.28 3.38	3.05%	11.34	15.83
GNR_2	33.04 33.04	0%	8.82 8.69	−1.8%	3.75 3.80	1.3%	9.49	15.69
GNR_3	36.98 32.80	−11.3%	9.03 8.33	−7.8%	4.10 3.94	−3.9%	14.03	13.04
GNR_4	33.95 32.25	−5%	8.73 8.29	−5%	3.89 3.89	0%	8.16	9.55

Table 4.1: The size parameters of the gold nanorod and silica shell used in the single GNR modeling. L_{r}, W_{r} and AR_{r} are the length, width and aspect ratio of the nanorod, respectively. The "m" correspond to *measured* dimensions of a TEM measurements and the "f" correspond to *fitted* dimensions to the size parameters used in the computational model to fit into experimental data. L_{tip} and L_{mid} are the silica shell thickness at the tip and in the half length of the gold nanorod, respectively. e_{L}, e_{W} and e_{AR} corresponds to the percent error between measured and fitted dimensions.

The experimental extinction cross-sections of 4 gold nanorods (Figure 3.7) are shown as a black circles in Figures 4.4 - 4.7. An extinction cross-section of a single gold nanorod modeled with the dimensions measured during TEM imaging (see Table 4.1) and a size corrections to the bulk dielectric function given in Table 4.2, are shown as a dashed lines

Name	$V\left[\frac{\text{meas.}}{\text{fitted}}\right]$ $(\cdot 10^{-24}$ m$^3)$	$S\left[\frac{\text{meas.}}{\text{fitted}}\right]$ $(\cdot 10^{-16}$ m$^2)$	$L_{\mathrm{eff}}\left[\frac{\text{meas.}}{\text{fitted}}\right]$ (nm)	$A\left[\frac{\text{meas.}}{\text{fitted}}\right]$
GNR_1	2.61 1.98	11.5 9.67	9.03 8.19	0.9 0.46
GNR_2	1.81 1.76	9.12 8.96	7.97 7.86	0.5 0.47
GNR_3	2.13 1.74	10.4 8.94	8.22 7.78	0.6 0.54
GNR_4	1.83 1.57	9.26 8.36	7.91 7.52	0.8 0.55

Table 4.2: Parameters used in the size corrections for bulk dielectric function of gold. V, S, L_{eff} and A are volume and surface area of the nanorod, effective mean free path and broadening parameter for the *measured* and *fitted* FEM model, respectively.

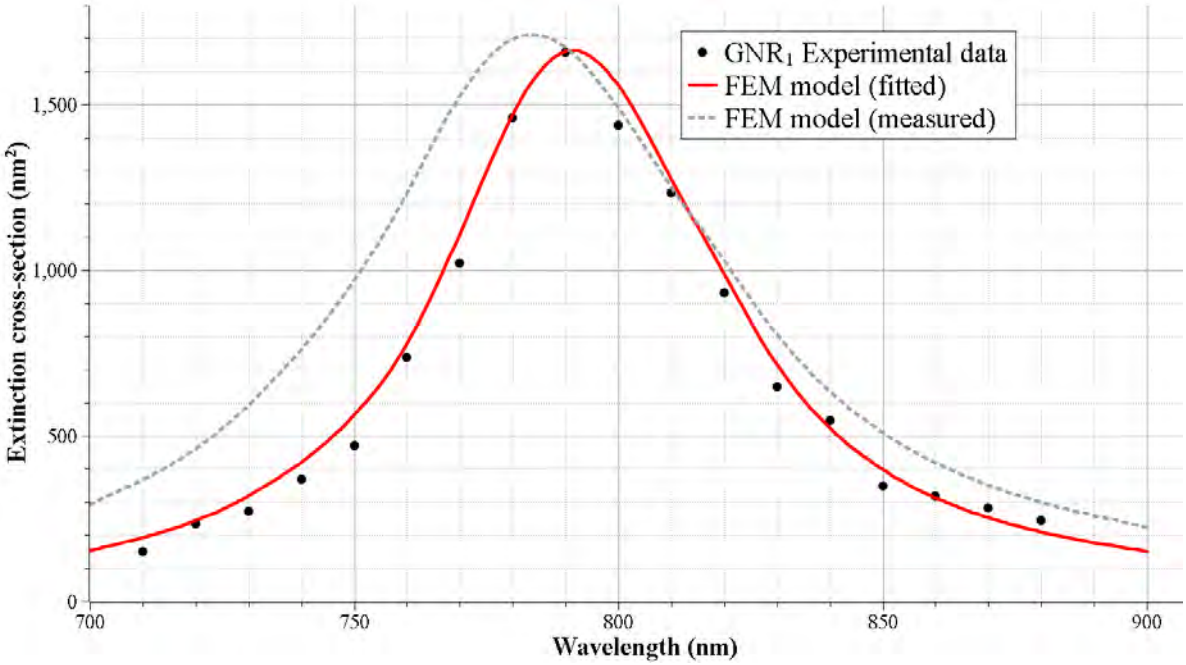

Figure 4.4: Experimental and simulated extinction cross-sections of GNR_1

in the Figures 4.4 - 4.7.

Parameters used for size corrections of the bulk dielectric function of gold (equation 2.40) for measured and fitted extinction spectrum simulations (Figures 4.4 - 4.7) are given in the Table 4.2.

GNR_1

Since the simulated extinction spectrum, using the measured size parameters and size corrected dielectric function for gold, was blue shifted and had a FWHM wider than an experimental spectrum (dashed line, Figure 4.4), the dimensions of the GNR in the simulation were modified as described in the section 3.4 to the size given in the Table 4.1 (fitted). The fitted extinction cross-section from the simulation with modified dimensions of the GNR_1 and size corrections to the dielectric function of gold from the Table 4.2 is shown as a red line in Figure 4.4. As shown with the red line in Figure 4.4, using the fitted size parameters, the simulated spectrum quantitatively fits very well with experimental values of the extinction cross-section from a single gold nanorod measurement. The difference in FWHMs of the simulated and experimental spectra is 5% (63 nm for

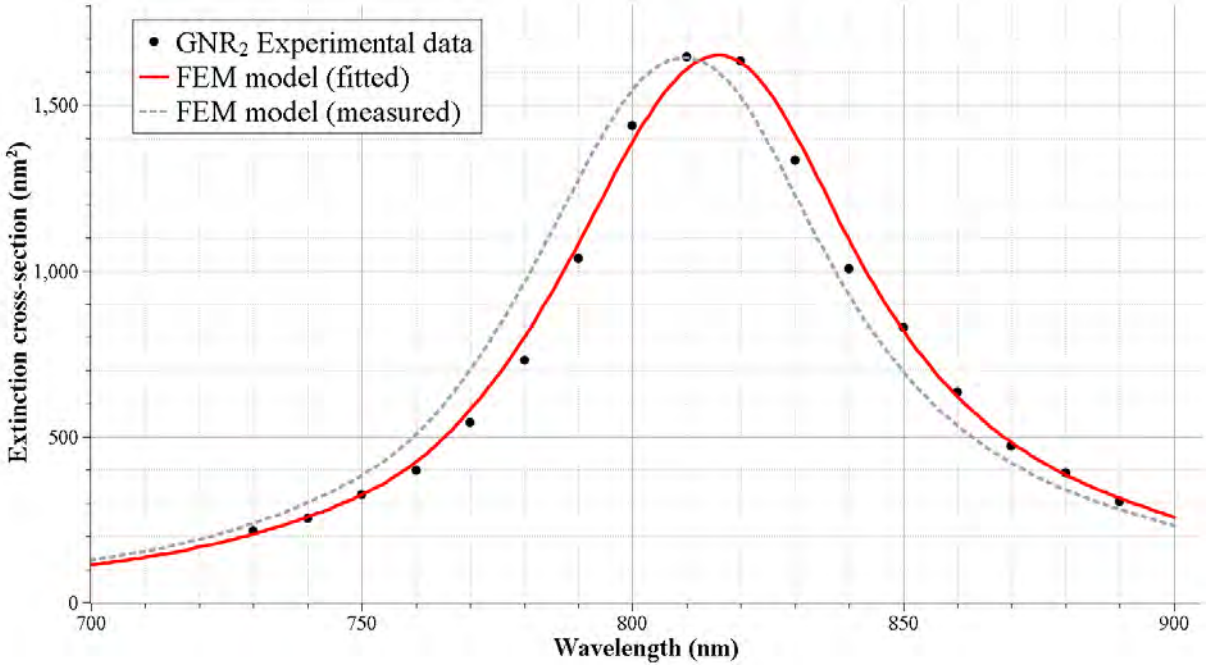

Figure 4.5: Experimental and simulated extinction cross-sections of GNR_2

simulated and 60 nm for experimental spectra).

GNR_2

To fit extinction cross-section of GNR_2 to the experimental spectrum, less modifications were required. Again as was described above, in the example of GNR_1, to align resonance peak position, the dimensions of the GNR in the simulation were modified as described in the section 3.4 to the size given in the Table 4.1 (fitted). Size corrected dielectric function of gold for the GNR_2 was modified according to the parameters given in the Table 4.2. The red line in the Figure 4.5 shows the results of the fitting with difference in FWHMs of 4.5% (69 nm for simulated and 66 nm for experimental spectra).

GNR_3

Similar steps, as described in the previous two cases, were repeated to fit the simulated extinction cross-section of the GNR_3 with the experimental spectrum. The red line in the Figure 4.6 shows the results of the fitting with a FWHMs of 75.8 nm for the simulated

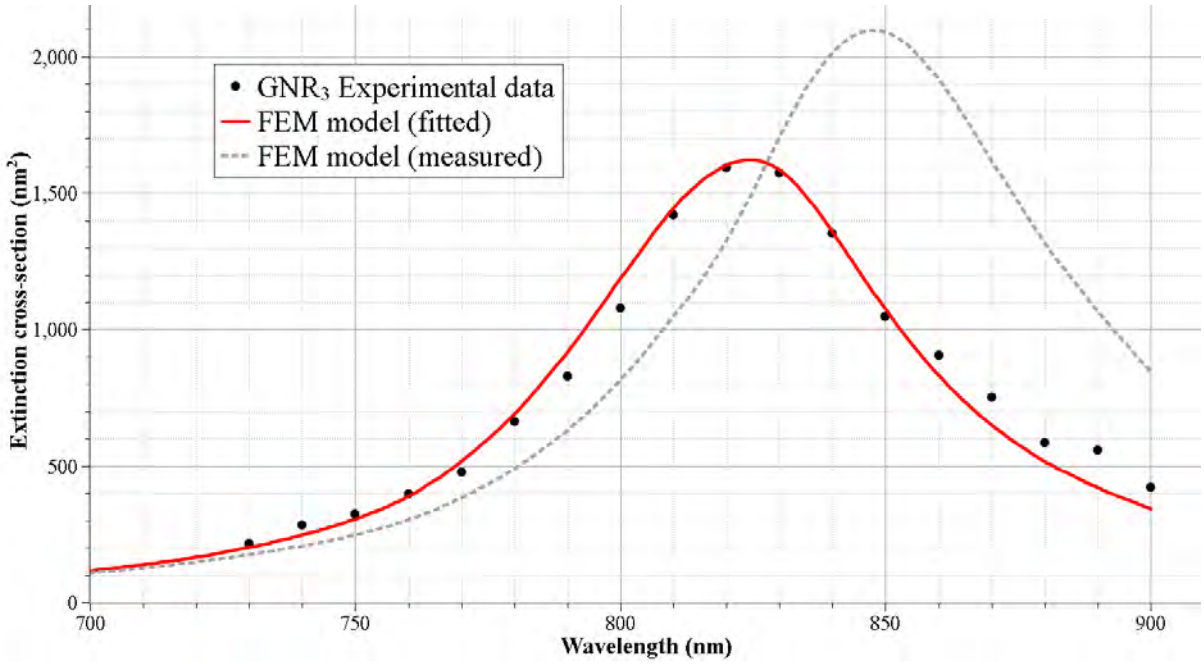

Figure 4.6: Experimental and simulated extinction cross-sections of GNR_3

and 76.4 nm for the experimental spectra.

GNR_4

For the model of the GNR_4, only the size of the nanorod was decreased by 5% (see Table 4.1 (fitted)) leaving the same aspect ratio of the nanorod. The red line in the Figure 4.7 shows the fitted extinction spectrum from the FEM model. Both the fitted simulated and experimental extinction cross-sections have the same FWHMs of 74 nm.

4.4 Discussion

A three-dimensional finite element model was built to mimic the experimental setup of SMS. Although the experimental setup consisted of an unbounded domain the computational model, due to finite resources, had to be truncated with appropriate boundary conditions. Two types of boundary conditions that can be used are an absorbed boundary condition (ABC) with a perfectly matched layer (PML) and perfect electrical conductor (PEC) with perfect magnetic conductor (PMC). While the absorbing boundary condi-

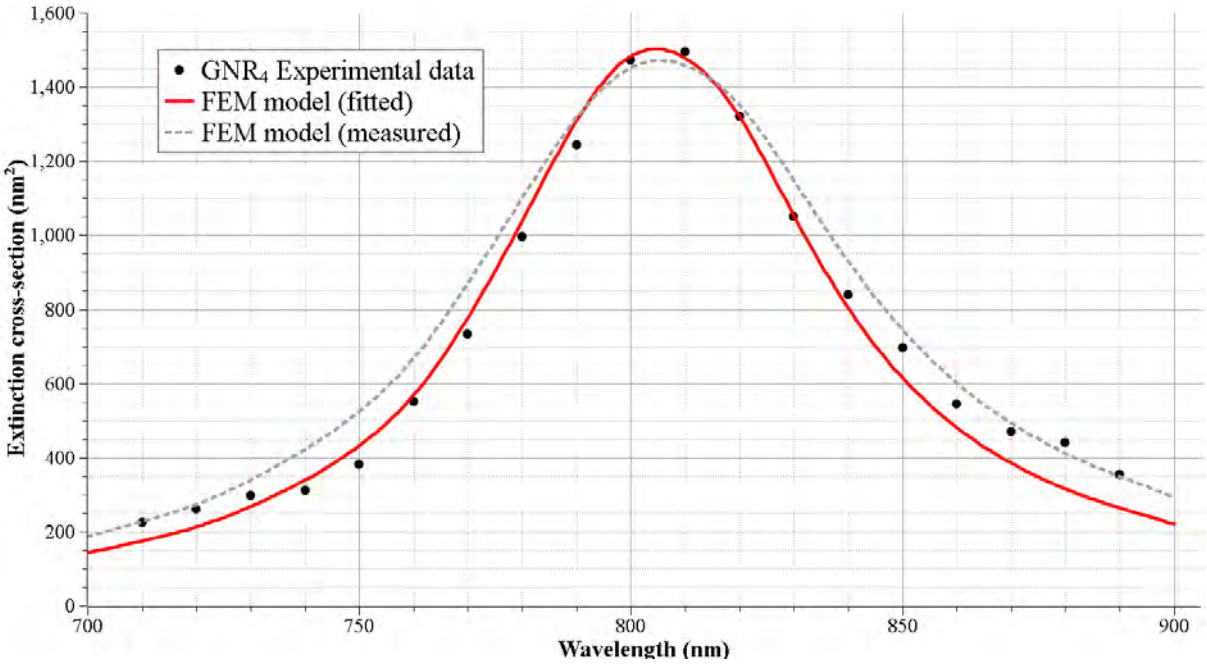

Figure 4.7: Experimental and simulated extinction cross-sections of GNR_4

tion and perfectly matched layers provide boundaries where electromagnetic waves will be strongly attenuated with minimal reflections, the PEC and PMC provide periodicity and hence infinity of the domain at the boundary. Initial testing of the ABC+PML boundaries to truncate computational domain showed excellent results in the simulations of the electromagnetic wave propagation in the homogeneous environment, but revealed a strong scattering component of the electromagnetic wave in simulations where the substrate was adjacent to the boundary. PEC/PMC conditions on the other hand produced an excellent results for the truncation of the computational domain where the substrate was adjacent to the boundary. The use of PEC/PMC conditions on the boundaries for non-periodic structures must be used with care since too close positioning of the boundaries to the scatter can bring artifacts to the solution due to near field coupling effects of the periodic structures.

In our model, PEC/PMC boundaries were placed 700 nm away from the center of the computational domain and were tested against an analytical solution for the sphere (Figure 4.1). An excellent agreement of the analytical and FEM solution was achieved by placing PEC/PMC boundaries sufficiently far so that any further increase of the domain

size did not affect the solution. The meshing of the computational domain was done with the use of at least 10 linear elements per wavelength where the solution did not expect to vary rapidly and finner refinement of the plasmonic nanostructures.

The current model for a single nanoparticle characterization is limited for the use with nanostructures, due to the assumptions made in section 3.3, where absorption dominates over scattering. In the case of the gold nanospheres and the gold nanorods the main contribution to the scattering coming from the radiation damping. It was shown by Sönnichsen *et. al.* [49] (see Figure 2.6) that the scattering cannot be neglected for the gold nanospheres with diameter wider than 40 nm, where radiation damping Γ_{rad} starts to contribute to the overall damping processes. Novo *et. al.* [39] (see Figure 2.7) showed that the radiation damping becomes dominant for the gold nanorods with L_{eff} wider than 17 nm, setting up a limitation for our model before including scattering cross-section calculations for a single gold nanorod or radiation damping into the dielectric function of gold.

The sensitivity of the model was tested and the experimental validation was done by comparison of the spectrophotometry measurements of a colloidal solution before and after coating of the GNRs with predictions of the FEM model of a single gold nanorod with and without silica coating (Figure 4.2). A 23 nm longitudinal peak position shift was observed experimentally due to coating of the GNRs with $\approx$ 20 nm silica shell thickness. The 23 nm was observed in the FEM modeling of the average size GNR with and without a 20 nm silica shell. The differences in the FWHMs between the experimental and FEM spectra are due to the distribution of the GNRs dimensions (Figure 3.2), which affects the FWHM of the extinction spectrum. To more closely represent the spectrophotometry measurements in the FEM model, several GNR's dimensions should be modeled and averaged weighted into one extinction spectrum by the statistical distribution.

For validation of the FEM model against a single gold nanorod spectrum, 4 silica coated GNRs were measured with SMS (Figures 4.4 - 4.7) and imaged with TEM (Figure 3.7). Silica coated GNRs were preferable since the silica shell provides a more controllable environment than the uncertain amount of surfactant molecule on the nanorod and surface of the substrate.

The uncertainty in the TEM characterization of the gold nanorods was up to 30%. The percentage errors (see Table 3.1) between fit dimensions of the nanorod needed to match the experimental spectrum and the dimensions measured during TEM measurements are

smaller than uncertainties in the TEM characterization and lies within 11% error margin. GNR_2 needed the least alterations in the size of the gold nanorod. This may be due to the higher magnification used during TEM of the nanorod's dimensions. In modeling of the GNR_1, GNR_3 and GNR_4 just minor alterations of the dimensions were needed to obtain good quantitative fit to the experimental data, having the same extinction peak position and spectral shape.

One of the main aims of the single GNR model validation was evaluation of the size corrections to the Drude-like dielectric function of gold. Experimental data obtained during optical characterization of single gold nanorods was used to determine the broadening parameter A, which corresponds to electron surface scattering due to the limited mean free path of electrons between collisions. Comparison of the dimensions in the Table 4.2 for the fitted FEM model also shows similar values for the obtained A, since broadening parameter A accounts for an additional scattering of the conduction electrons from the nanorod's surface (see section 2.2.4) and for the similar geometry and size of the nanoparticle assumed to be comparable.

Obtained values for A, are similar to what is reported in the literature. Quinten [61] in his calculations deduced $A = 0.6$ for spherical gold clusters with the mean radius of 8 nm which is within the range of our particles size. Novo *et. al.* [39] determined that $A = 0.3$ for single uncoated gold nanorod in solution with width ranging from 8 to 14 nm. Sönnichsen *et. al.* [38] calculated $A = 0.5$ for gold nanorods with diameters of $15-25$ nm and having aspect ratios from 2 to 4. In their experiments extinction from a single gold uncoated nanorod was obtained but no size correlation with imaged particles was done. Berciaud *et. al.* [62] in their experiments with individual spherical nanoparticles with diameter between 33 to 5 nm, used Mie theory to deduce that $A = 0.25$. Therefore, the obtained values for A are consistent with those obtained elsewhere. Deviations can rise from the differences in the way the data was obtained. All literature values were obtained for uncoated gold nanorods or spheres embedded in a homogeneous environment of water without correlation at the single gold nanoparticle level, while in our experimental setup, gold nanorods were correlated at a single GNR level.

The broadening parameter A is an empirical value that can be used in the simulations of uncoated/coated gold nanorods with similar dimensions.

Chapter 5

Summary, conclusion and future work

5.1 Summary

In this thesis two aims were pursued and accomplished.

The first was to build a theoretical model that can predict optical response of a single nanorod due to interaction with an electromagnetic wave. The second was the use of SMS and TEM to experimentally characterize single gold nanorod and evaluate size corrections to the bulk dielectric function of gold with the use of the FEM model.

To accomplish these aims a three-dimensional finite element model of an actual SMS experimental setup was built. To test for possible numerical errors in the model, it was tested against an analytical solution of Mie scattering which showed excellent agreement. Furthermore, to test the model sensitivity, it was tested against spectrophotometer experimental data for a colloidal solutions of gold nanorods. The model precisely predicted the slight shift in the resonance peak position due to the silica coating of gold nanorods. The use of bulk dielectric function of gold is limited to very big clusters and inapplicable at a nanoscale if good quantitative results are to be achieved. Due to the dimensions of the gold nanorods investigated in this thesis, the dielectric function of gold becomes size-dependent. The evaluation of the size corrections to the bulk dielectric function of gold was showed the good quantitative agreement between the modeled and experimentally obtained extinction cross-sections of a single nanorod with TEM size correlation. The

obtained size-corrected dielectric function of gold can be used for further investigations of same size gold nanorod behavior in different dielectric environments.

5.2 Conclusions

Plasmonic nanoparticles attract a large amount of interest in researchers from varying areas. Improvements in synthesis and experimental characterization of nanoparticles motivate a deeper understanding of the theory that stands behind the optical and material properties of particles at nanoscale. In this thesis, for the first time theory and experimental techniques were applied for the quantitative characterization of single gold nanorod optical properties by determining the size-corrections to the bulk dielectric function of gold.

It has been shown that the finite element method with the size dependent dielectric function of gold is capable of accurately predicting the optical behavior of a single gold nanorod. An experimental and theoretical characterization of a single nanoparticle with such techniques as SMS and FEM can validate the size correction parameters for the bulk dielectric function of gold. This finite element model is a powerful and useful tool for the design of new plasmonic sensors and therapeutic agents for biomedical applications.

5.3 Future Work

The established model can accurately predict the scattering and absorption properties of nanoparticles embedded in a homogeneous environment. It is also applicable to the structures placed on top of the dielectric substrate, where absorption dominates over scattering and scattering can be neglected in the extinction cross-section measurements. The incorporation of scattering cross-section calculations in the model is needed to extend applicability of this model to highly scattering nanostructures on top of a substrate.

The SMS is a far-field spectroscopy technique, where transmitted light (scattered and absorbed) is collected by 106° aperture. To calculate scattering cross-section of the nanoparticle, it is needed to account for scattered radiation in the far-field over 254° spherical boundary and subtract scattered far-field in the absence of the particle from the scattered far-field due to the nanoparticles presents.

The possible way to address this task is to use Stratton-Chu formulas with substrate fully incorporated inside and not reaching boundaries of the integration sphere. The possible challenge of this model is to find region where the solution stop changing with increasing of the substrate size.

Another way to incorporate scattering cross-sections calculations is to use Stratton-Chu formulas only at regions of a hemi-sphere above and below of the substrate, leaving region of the substrate outside of the integration.

Since most of the individual gold nanorods that were imaged to obtain the size correction for the dielectric function had more or less the same dimensions it is very important to experimentally image and then simulate a wide range of gold nanorods dimensions and aspect ratios in order to build a map of broadening parameters.

As mentioned in the discussion section, the current model uses PEC/PMC as a truncation boundary for the domains, which represents a periodic structure. To eliminate this limitation the future model should be developed with optimized ABC+PML conditions.

When tested with uncoated nanorods, the current model had discrepancies between the experimental and theoretical spectra. This may have been due to leftover surfactant molecule and/or water on the surface of the nanorod and substrate. To overcome this limitation in the future an additional layer that will present the effect of the surfactant molecule should be added. Another way is to optimize the experimental technique by placing a TEM grid after spin coating of the colloidal solution into an oven to dry out any water content at the surface of the grid.

References

[1] Chiche A., Skowronek J., Kubaszewska M., and Kanikowski M. Hyperthermia - description of a method and a review of clinical applications. *Reports of Practical Oncology and Radiotherapy*, 12(5):267–275, 2007.

[2] Chaussy C. and Throff S. High-intensity focused ultrasound in the management of prostate cancer. *Expert Review of Medical Devices*, 7(2):209–217, 2010.

[3] Kimura M., Baba S., and Polascik T.J. Minimally invasive surgery using ablative modalities for the localized renal mass: Review article. *International Journal of Urology*, 17(3):215–227, 2010.

[4] Van Bezooijen B.P.J., Horenblas S., Meinhardt W., and Newling D.W.W. Interstitial microwave thermal therapy for prostate cancer: Method of treatment and results of a phase I/II trial. *Journal of Urology*, 166(5):1707–1714, 2001.

[5] Vogl T.J., Straub R., Eichler K., Woitaschek D., and Mack M.G. Laser-induced interstitial thermotherapy (LITT) and local ablative techniques. *Therapeutische Umschau*, 58(12):718–725, 2001.

[6] Zhang J.Z. and Noguez C. Plasmonic optical properties and applications of metal nanostructures. *Plasmonics*, 3(4):127–150, 2008.

[7] Jain P.K., Huang X., El-Sayed I.H., and El-Sayed M.A. Noble metals on the nanoscale: Optical and photothermal properties and some applications in imaging, sensing, biology, and medicine. *Accounts of Chemical Research*, 41(12):1578–1586, 2008.

[8] Huang X., Jain P.K., El-Sayed I.H., and El-Sayed M.A. Gold nanoparticles: Interesting optical properties and recent applications in cancer diagnostics and therapy. *Nanomedicine*, 2(5):681–693, 2007.

[9] Yao C.-P., Zhang Z.-X., and Yao B.-L. Laser irradiation cell photothermal therapy assisted by gold nanoparticles. *Progress in Biochemistry and Biophysics*, 34(3):312–316, 2007.

[10] El-Sayed I.H., Huang X., and El-Sayed M.A. Selective laser photo-thermal therapy of epithelial carcinoma using anti-EGFR antibody conjugated gold nanoparticles. *Cancer Letters*, 239(1):129–135, 2006.

[11] Dickerson E.B., Dreaden E.C., Huang X., El-Sayed I.H., Chu H., Pushpanketh S., McDonald J.F., and El-Sayed M.A. Gold nanorod assisted near-infrared plasmonic photothermal therapy (PPTT) of squamous cell carcinoma in mice. *Cancer Letters*, 269(1):57–66, 2008.

[12] Terentyuk G.S., Maslyakova G.N., Suleymanova L.V., Khlebtsov N.G., Khlebtsov B.N., Akchurin G.G., Maksimova I.L., and Tuchin V.V. Laser-induced tissue hyperthermia mediated by gold nanoparticles: toward cancer phototherapy. *Journal of biomedical optics*, 14(2):021016, 2009.

[13] El-Sayed I.H. Nanotechnology in head and neck cancer: The race is on. *Current Oncology Reports*, 12(2):121–128, 2010.

[14] Huang X., Jain P.K., El-Sayed I.H., and El-Sayed M.A. Plasmonic photothermal therapy (PPTT) using gold nanoparticles. *Lasers in Medical Science*, 23(3):217–228, 2008.

[15] Loo C., Lin A., Hirsch L., Lee M.-H., Barton J., Halas N., West J., and Drezek R. Nanoshell-enabled photonics-based imaging and therapy of cancer. *Technology in Cancer Research and Treatment*, 3(1):33–40, 2004.

[16] Huang X., Qian W., El-Sayed I.H., and El-Sayed M.A. The potential use of the enhanced nonlinear properties of gold nanospheres in photothermal cancer therapy. *Lasers in Surgery and Medicine*, 39(9):747–753, 2007.

[17] Pissuwan D., Valenzuela S.M., Killingsworth M.C., Xu X., and Cortie M.B. Targeted destruction of murine macrophage cells with bioconjugated gold nanorods. *Journal of Nanoparticle Research*, 9(6):1109–1124, 2007.

[18] Cole J.R., Mirin N.A., Knight M.W., Goodrich G.P., and Halas N.J. Photothermal efficiencies of nanoshells and nanorods for clinical therapeutic applications. *Journal of Physical Chemistry C*, 113(28):12090–12094, 2009.

[19] Von Maltzahn G., Park J.-H., Agrawal A., Bandaru N.K., Das S.K., Sailor M.J., and Bhatia S.N. Computationally guided photothermal tumor therapy using long-circulating gold nanorod antennas. *Cancer Research*, 69(9):3892–3900, 2009.

[20] Alekseeva A.V., Bogatyrev V.A., Khlebtsov B.N., Melnikov A.G., Dykman L.A., and Khlebtsov N.G. Gold nanorods: Synthesis and optical properties. *Colloid Journal*, 68(6):661–678, 2006.

[21] Pérez-Juste J., Pastoriza-Santos I., Liz-Marzán L.M., and Mulvaney P. Gold nanorods: Synthesis, characterization and applications. *Coordination Chemistry Reviews*, 249(17-18 SPEC. ISS.):1870–1901, 2005.

[22] Ungureanu C., Rayavarapu R.G., Manohar S., and Van Leeuwen T.G. Discrete dipole approximation simulations of gold nanorod optical properties: Choice of input parameters and comparison with experiment. *Journal of Applied Physics*, 105(10), 2009.

[23] Huang X., El-Sayed I.H., Qian W., and El-Sayed M.A. Cancer cell imaging and photothermal therapy in the near-infrared region by using gold nanorods. *Journal of the American Chemical Society*, 128(6):2115–2120, 2006.

[24] Tsukerman I. *Computational methods for nanoscale applications: particles, plasmons and waves*. Springer, 2008.

[25] Draine B.T. and Flatau P.J. Discrete-dipole approximation for scattering calculations. *Journal of the Optical Society of America A: Optics and Image Science, and Vision*, 11(4):1491–1499, 1994.

[26] Draine B.T. and Flatau P.J. User guide for the discrete dipole approximation code DDSCAT 7.1. *arXiv:1002.1505v1 [astro-ph.IM]*, 2010.

[27] Draine B.T. and Flatau P.J. Discrete-dipole approximation for periodic targets: Theory and tests. *Journal of the Optical Society of America A: Optics and Image Science, and Vision*, 25(11):2693–2703, 2008.

[28] Jackson J.D. *Classical electrodynamics, 3rd ed.* John Wiley Sons, Inc., 1999.

[29] Yee K. Numerical solution of initial boundary value problems involving maxwell's equations in isotropic media. *IEEE Transactions on Antennas and Propagation*, 14(3):302–307, 1966.

[30] Oh M.K., Park S., Kim S.K., and Lim S.-H. Finite difference time domain calculation on layer-by-layer assemblies of close-packed gold nanoparticles. *Journal of Computational and Theoretical Nanoscience*, 7(6):1085–1094, 2010.

[31] Atkinson A.L., Mcmahon J.M., and Schatz G.C. FDTD studies of metallic nanoparticle systems. *NATO Science for Peace and Security Series A: Chemistry and Biology*, pages 11–32, 2009.

[32] Pelosi G. The finite-element method, part i: R. L. Courant. *IEEE Antennas and Propagation Magazine*, 49(2):180–182, 2007.

[33] Silvester P. Finite-element solution of homogeneous waveguide problems. *Alta Frequenza*, 38, 1969.

[34] Arlett P.L., Bahrani A.K., and Zienkiewicz O.C. Application of finite elements to the solution of Helmholtz's equation. *Proc. IEE*, 115(12):1762–1766, 1968.

[35] Jianming Jin. *The Finite Element Method in Electromagnetics, 2nd Edition.* Wiley-IEEE Press, 2002.

[36] Volakis J.L., Chatterjee A., and Kempel L.C. *Finite element method for electromagnetics: antennas, microwave circuits, and scattering applications.* Wiley-IEEE Press, 1998.

[37] Monk P. *Finite element methods for Maxwell's equations*. Oxford University Press, 2003.

[38] Sönnichsen C., Franzl T., Wilk T., Von Plessen G., Feldmann J., Wilson O., and Mulvaney P. Drastic reduction of plasmon damping in gold nanorods. *Physical Review Letters*, 88(7):774021–774024, 2002.

[39] Novo C., Gomez D., Pérez-Juste J., Zhang Z., Petrova H., Reismann M., Mulvaney P., and Hartland G.V. Contributions from radiation damping and surface scattering to the linewidth of the longitudinal plasmon band of gold nanorods: A single particle study. *Physical Chemistry Chemical Physics*, 8(30):3540–3546, 2006.

[40] Arbouet A., Christofilos D., Del Fatti N., Valle F., Huntzinger J.R., Arnaud L., Billaud P., and Broyer M. Direct measurement of the single-metal-cluster optical absorption. *Physical Review Letters*, 93(12):127401–1–127401–4, 2004.

[41] Muskens O.L., Bachelier G., Del Fatti N., Valle F., A. Brioude, X. Jiang, and Pileni M.-P. Quantitative absorption spectroscopy of a single gold nanorod. *Journal of Physical Chemistry C*, 112(24):8917–8921, 2008.

[42] Maier S.A. *Plasmonics: fundamentals and applications*. Springer, 2007.

[43] Wooten F. *Optical Properties of Solids*. New York City: Academic Press, 1972.

[44] Johnson P.B. and Christy R.W. Optical constants of the noble metals. *Physical Review B*, 6(12):4370–4379, 1972.

[45] Kreibig U. and Vollmer M. *Optical Properties of Metal Clusters*. Springer, 1995.

[46] Blackman J.A. *Metallic nanoparticles*. Elsevier, 2009.

[47] Pinchuk A., Von Plessen G., and Kreibig U. Influence of interband electronic transitions on the optical absorption in metallic nanoparticles. *Journal of Physics D: Applied Physics*, 37(22):3133–3139, 2004.

[48] Coronado E.A. and Schatz G.C. Surface plasmon broadening for arbitrary shape nanoparticles: A geometrical probability approach. *Journal of Chemical Physics*, 119(7):3926–3934, 2003.

[49] Sönnichsen Carsten. *Plasmons in metal nanostructures*. PhD thesis, Ludwig-Maximilians-Universitt Mnchen, 2001.

[50] Sönnichsen C., Franzl T., Wilk T., Von Plessen G., and Feldmann J. Plasmon resonances in large noble-metal clusters. *New Journal of Physics*, 4:93.1–93.8, 2002.

[51] Muskens O., Christofilos D., Del Fatti N., and Valle F. Optical response of a single noble metal nanoparticle. *Journal of Optics A: Pure and Applied Optics*, 8(4):S264–S272, 2006.

[52] Muskens O., Del Fatti N., and Valle F. Absorption spectroscopy and identification of single metal nanoparticles. volume 5927, pages 1–10, 2005.

[53] Mie G. Beitrage zur optik trber medien, speziell kolloidaler metallösungen. *Annalen der Physik*, 25(3):377–445, 1908.

[54] Maioli P. SigmaMie 1.05. CNRS, Universite Claude Bernard Lyon 1, France.

[55] Fernández-Lopéz C., Mateo-Mateo C., Alvarez-Puebla R.A., Pérez-Juste J., Pastoriza-Santos I., and Liz-Marzán L.M. Highly controlled silica coating of peg-capped metal nanoparticles and preparation of sers-encoded particles. *Langmuir*, 25(24):13894–13899, 2009.

[56] Stratton J.A. and Chu L.J. Diffraction theory of electromagnetic waves. *Physical Review*, 56(1):99–107, 1939.

[57] COMSOL Version 3.5a. *Comsol Multiphysics User's Guide*. COMSOL, 2009.

[58] Mikhailovsky A.A., Petruska M.A., Stockman M.I., Bartko A., Achermann M., and Klimov V.I. Near-field, phase-sensitive spectroscopy of metal nanoassemblies. volume 89, pages QTUA2/1–QTUA2/2, 2003.

[59] Mock J.J., Barbic M., Smith D.R., Schultz D.A., and Schultz S. Shape effects in plasmon resonance of individual colloidal silver nanoparticles. *Journal of Chemical Physics*, 116(15):6755–6759, 2002.

[60] Del Fatti N., Christofilos D., and Valle F. Optical response of a single gold nanoparticle. *Gold Bulletin*, 41(2):147–158, 2008.

[61] Quinten M. Optical constants of gold and silver clusters in the spectral range between 1.5 eV and 4.5 eV. *Zeitschrift fur Physik B-Condensed Matter*, 101(2):211–217, 1996.

[62] Berciaud S., Cognet L., Tamarat P., and Lounis B. Observation of intrinsic size effects in the optical response of individual gold nanoparticles. *Nano Letters*, 5(3):515–518, 2005.